

The active weak-line T Tauri star LkCa 4 observed with SPIRou and TESS

B. Finociety¹ *, J.-F. Donati¹, K. Grankin², J. Bouvier³, S. Alencar⁴, F. Ménéard³, T.P. Ray⁵,
Á. Kóspál⁶ and the SLS consortium

¹ *Université de Toulouse, CNRS, IRAP, 14 av. Belin, 31400 Toulouse, France*

² *Crimean Astrophysical Observatory, 298409 Nauchny, Republic of Crimea*

³ *Université Grenoble Alpes, CNRS, IPAG, F-38000 Grenoble, France*

⁴ *Departamento de Física - ICEx - UFMG, Av. Antonio Carlos 6627, 30270-901 Belo Horizonte, MG, Brazil*

⁵ *Dublin Institute for Advanced Studies, Dublin, Ireland*

⁶ *Konkoly Observatory, Research Centre for Astronomy and Earth Sciences, Konkoly-Thege Miklós út 15-17, 1121 Budapest, Hungary*

Accepted 2023 January 23. Received 2023 January 23; in original form 2022 November 25

ABSTRACT

We report results of a spectropolarimetric and photometric monitoring of the weak-line T Tauri star LkCa 4 within the SPIRou Legacy Survey large programme, based on data collected with SPIRou at the Canada-France-Hawaii Telescope and the TESS space probe between October 2021 and January 2022. We applied Zeeman-Doppler Imaging to our spectropolarimetric and photometric data to recover a surface brightness distribution compatible with TESS photometry, as well as the large-scale magnetic topology of the star. As expected from the difference in wavelength between near-infrared and optical data, the recovered surface brightness distribution is less contrasted than the previously published one based on ESPaDOnS data, but still features mid-latitude dark and bright spots. The large-scale magnetic field is consistent in shape and strength with the one derived previously, with a poloidal component resembling a 2.2 kG dipole and a toroidal component reaching 1.4 kG and encircling the star at the equator. Our new data confirm that the surface differential rotation of LkCa 4 is about 10 times weaker than that of the Sun, and significantly different from zero. Using our brightness reconstruction and Gaussian Process Regression, we were able to filter the radial velocity activity jitter down to a precision of 0.45 and 0.38 km s⁻¹ (from an amplitude of 6.10 km s⁻¹), respectively, yielding again no evidence for a close-in massive planet orbiting the star.

Key words: techniques: polarimetric – stars: activity – stars: imaging – stars: individual: LkCa 4 – stars: magnetic field

1 INTRODUCTION

At an age of a few Myr, young low-mass stars ($M_* < 2 M_\odot$) emerge from their dust cocoon and become T Tauri stars (TTSs). These pre-main sequence (PMS) stars are still undergoing a phase of contraction towards the main sequence (MS). One distinguishes two kinds of TTSs, the classical T Tauri stars (cTTSs) accreting material from the circumstellar disc in which planets are in the process of formation, and the weak-line T Tauri stars (wTTSs), the accretion disc of which has mostly dissipated. TTSs are key targets to constrain theoretical models of stellar and planetary formation.

In particular, studying the magnetic field of these stars is of crucial importance given the essential role it plays at early stages of stellar evolution, controlling the accretion/ejection process at work in cTTSs and therefore angular momentum evolution of TTSs (Bouvier et al. 2007; Frank et al. 2014). Thanks to high-resolution spectropolarimeters such as ESPaDOnS (Donati 2003), on the 3.6m Canada-France-Hawaii Telescope (CFHT), a small sample of cTTSs has been studied over the last two decades. These studies reveal that cTTSs host strong large-scale magnetic fields of a few hundred gauss to a few kilogauss (e.g. Donati et al. 2007, 2011, 2013; Alencar et al. 2012; Bouvier et al. 2020), the topology of which mainly reflects

the internal structure of the star (Donati & Landstreet 2009; Morin et al. 2010; Gregory et al. 2012). More specifically, the topology is more complex and departs from a low-order, mainly axisymmetric poloidal field when the star becomes largely radiative.

WTTSs are also targets of interest for further constraining stellar and planetary evolution models, as TTSs evolve from cTTSs to wTTSs and post TTSs. A Large Programme named ‘Magnetic Topologies of Young Stars and the Survival of close-in giant Exoplanets’ (MaTYSSSE) carried out with ESPaDOnS, was dedicated to the observation of a few tens of wTTSs to study their large-scale magnetic fields and investigate how different they are compared to those hosted by cTTSs. Studies carried out as part of the MaTYSSSE programme showed that most wTTSs follow magnetic trends similar to those of cTTSs, i.e. with strong, simple and mostly axisymmetric large-scale poloidal fields when the star is fully convective. However, some depart from this picture like, e.g., the fully convective stars V410 Tau (Yu et al. 2019; Finociety et al. 2021) and LkCa 4 (Donati et al. 2014) that also exhibit a strong toroidal field. Another goal of MaTYSSSE was to search for close-in massive planets (called hot Jupiters/hJs) orbiting wTTSs, in order to constrain evolutionary models at early stages of planet formation. This effort led to the detection of hJs around 2 wTTSs, namely TAP 26 (Yu et al. 2017) and V830 Tau (Donati et al. 2017), through the periodic modulation of

* E-mail: benjamin.finociety@irap.omp.eu

the radial velocity (RV) of the host star induced by the presence of these massive planets.

New opportunities to investigate the properties of TTSs came with the recently installed near-infrared (NIR) high-resolution spectropolarimeter and high-precision velocimeter SPIRou (Donati et al. 2020) at CFHT. In particular, the SPIRou Legacy Survey (SLS) Large Programme, allocated 310 nights at CFHT, includes a work package dedicated to the study of large-scale magnetic fields of cTTSs and wTTSs, and to the detection of hJs around such stars. As the Zeeman effect is enhanced at NIR wavelengths with respect to the optical domain, SPIRou is especially well suited for magnetic studies of TTSs, that are also often brighter in this spectral range. Moreover, we expect the RV activity jitter induced by the star itself to be smaller in the NIR thanks to the lower brightness contrast between surface features (spots, plages) and the quiet photosphere (e.g. Mahmud et al. 2011; Crockett et al. 2012), making it easier to detect the potential presence of close-in massive planets around these very active stars.

In this paper, we focus on the wTTS LkCa 4 we observed in the framework of SLS, in order to perform an analysis similar to that achieved for V410 Tau (Finociety et al. 2021). LkCa 4 is a young single fully-convective K7 wTTS (Herbig et al. 1986; Grankin 2013) with a logarithmic luminosity relative to the Sun of $\log L_*/L_\odot = -0.04 \pm 0.11$, an effective temperature and a logarithmic gravity of $T_{\text{eff}} = 4100 \pm 50$ K and $\log g = 3.8 \pm 0.1$ (Donati et al. 2014), located in the Taurus star-forming region (Herbig et al. 1986; White & Ghez 2001; Kraus et al. 2011; Grankin 2013) at a distance of 129.8 ± 0.3 pc (Gaia Collaboration et al. 2021). This star belongs to the C2-L1495 cloud, whose distance (129.53 pc) and age (1.34 ± 0.19 Myr) were recently estimated from GAIA data (Krolikowski et al. 2021). Using PMS evolution models of Siess et al. (2000), one finds that LkCa 4 is aged ~ 2 Myr, with a mass and a radius of $0.79 \pm 0.05 M_\odot$ and $2.0 \pm 0.2 R_\odot$, respectively (Donati et al. 2014). Using the more recent evolutionary models of Baraffe et al. (2015), we derive for LkCa 4 an age of ~ 1.3 Myr, consistent with that of the C2-L1495 cloud, along with a mass of $0.73 \pm 0.05 M_\odot$ and a radius of $1.9 \pm 0.2 R_\odot$. Given the distance, temperature and radius, and the visual extinction derived for this star ($A_V = 0.68 \pm 0.15$, Donati et al. 2014), we infer an unspotted V magnitude of 11.97 for LkCa 4, i.e., significantly brighter than the average observed V magnitude (12.624, Grankin et al. 2008), indicating that the star is heavily spotted. A recent study based on optical and NIR spectra further confirms this conclusion, suggesting that as much as 80% of surface of LkCa 4 may host dark brightness features (Gully-Santiago et al. 2017).

Based on optical data collected with ESPaDOnS in 2014 in the framework of the MaTYSSSE programme, our first study of LkCa 4 (Donati et al. 2014) concluded that the large-scale magnetic field of this star consists of a strong and simple, mostly axisymmetric, poloidal field (featuring a dipole component of 1.6 kG), and of a 1 kG toroidal component. In addition, the reconstructed brightness image features a dark polar spot as well as a warm plage at intermediate latitude that cover altogether about 25% of the visible surface. These features induce large photometric and velocimetric variations that were reasonably well modeled using tomographic techniques like Zeeman-Doppler Imaging (ZDI; Semel 1989; Brown et al. 1991; Donati & Brown 1997; Donati et al. 2006). The results of this study also illustrated that such techniques can mitigate the activity jitter in RV curves up to a RV precision of 0.055 km s^{-1} , and suggest that there is no hJ more massive than $1 M_{\text{jup}}$ orbiting LkCa 4 at a distance of 0.1 au or closer (i.e. no planet-induced RV signal with a semi-amplitude larger than 0.1 km s^{-1} was observed). Finally, Donati et al. (2014) also reported that the differential rotation (DR) at the

surface of LkCa 4 is much lower than that of the Sun, and potentially equal to 0 (solid-body rotation).

As a follow-up to this optical analysis, LkCa 4 has been monitored with SPIRou in the framework of the SLS from 2021 October 14 to 2022 January 30, contemporaneously with the Transiting Exoplanet Survey Satellite (TESS) from 2021 September 16 to November 06, during Sectors 43 and 44. Ground-based photometric measurements were also collected at the Crimean Astrophysical Observatory (CrAO) during the same observing period as SPIRou. We start this paper with a detailed description of our data set (Sec. 2). We then present the results obtained when applying ZDI to recover the brightness distribution and large-scale magnetic field at the surface of the star (Sec. 3). We investigate the activity of LkCa 4 with velocimetric measurements in Sec. 4 and through the study of three specific lines, known to be activity proxies in the NIR (the He I triplet at 1083.3 nm, the Paschen β and Brackett γ lines) in Sec. 5. We finally summarize and discuss our results in Sec. 6.

2 OBSERVATIONS

2.1 SPIRou observations

We observed LkCa 4 with SPIRou, collecting high-resolution spectra ranging from 950 to 2500 nm at a spectral resolving power of $\sim 70,000$ (Donati et al. 2020) between 2021 Oct 14 and 2022 Jan 30. Our dataset consists of 41 spectropolarimetric observations, each composed of a sequence of 4 subexposures of 550 s taken at different azimuths of the polarimeter retarder in order to remove (to first order) potential sources of spurious polarisation signals and systematic errors (Donati et al. 1997). These data were reduced using the LibreESPRIT pipeline, initially developed for ESPaDOnS (Donati et al. 1997), and adapted for SPIRou observations (Donati et al. 2020). Telluric correction was performed with a PCA approach similar to that outlined in Artigau et al. (2014). This yielded telluric-corrected spectra in both unpolarized (Stokes I) and circularly polarized (Stokes V) spectra, with a signal-to-noise ratio (SNR) per pixel in the H band ranging from 130 to 213 (median of 192). A full journal of observations is given in Table 1.

We applied Least-Square Deconvolution (LSD; Donati et al. 1997) to all our spectra, using a mask generated with the VALD-3 database (Ryabchikova et al. 2015) and containing only (moderate to strong) atomic lines with known Landé factor, and a relative depth (with respect to the continuum) of at least 3 per cent. This process provided Stokes I LSD profiles with average noise levels, expressed in units of the unpolarized continuum, ranging from 5.6×10^{-4} to 1.7×10^{-3} (median value of 6.7×10^{-4}) and Stokes V LSD profiles with average noise levels ranging from 1.8 to 3.4×10^{-4} (median of 2.1×10^{-4}). Strong Zeeman signatures are observed in Stokes V LSD profiles, with peak-to-peak amplitudes of typically 0.5%. The very obvious distortions in the shape of the Stokes I profiles indicate that large features are present at the stellar surface, which is further confirmed by the large amplitude of the photometric light curves (see Sec. 2.2).

We note that molecular lines located between 1500 and 1800 nm are affected by solar contamination. Applying LSD with a mask containing both atomic and molecular lines therefore does not improve and even degrades the SNRs of the Stokes I profiles; hence, we did not use such a mask for studying the brightness of LkCa 4 in contrast with what had been done for V410 Tau (Finociety et al. 2021).

Table 1. Spectropolarimetric observations of LkCa 4 collected with SPIRou between 2021 October and 2022 January. Columns 1 to 4 list the date, the Coordinated Universal Time, the Barycentric Julian Date and the rotation cycle (computed as indicated in Sec. 2.2.1). Columns 5 to 7 give the SNRs of the spectra in the *H* band, in the Stokes *I* and *V* LSD profiles while column 8 details the equivalent width of the Stokes *I* LSD profiles. From column 9 to 13, we list the measured RV, the longitudinal magnetic field, and the activity indicators, named EWVs (see Sec. 5), computed from the He I triplet at 1083.3 nm, Paschen β and Brackett γ lines, along with their error bars estimated from photon noise only (the number in parenthesis corresponds to the error bar taking into account intrinsic variability, see Sec. 5).

Date	UTC	BJD	Cycle	SNR	SNR _I	SNR _V	EW	RV	B _l	Activity proxies		
										He I (pm)	Pa β (pm)	Br γ (pm)
		2459000+					(km s ⁻¹)	(km s ⁻¹)	(G)			
2021 October 14	12:34:10	502.024	0.000	185	1285	4405	1.166 ± 0.016	2.000 ± 0.176	44 ± 16	3.9 ± 0.7 (5.4)	3.2 ± 0.8 (1.9)	-7.5 ± 2.6 (6.6)
2021 October 15	12:11:33	503.008	0.292	162	1094	3975	1.015 ± 0.016	-0.669 ± 0.209	227 ± 18	-2.2 ± 0.7 (5.4)	-3.6 ± 0.8 (1.9)	-5.1 ± 2.6 (6.6)
2021 October 19	13:49:55	507.076	1.498	205	1522	5180	1.341 ± 0.015	-1.327 ± 0.143	135 ± 13	-11.6 ± 0.7 (5.4)	-3.7 ± 0.8 (1.9)	-5.6 ± 2.6 (6.6)
2021 October 20	12:48:26	508.034	1.782	191	1503	4851	1.415 ± 0.015	0.766 ± 0.135	227 ± 13	-9.9 ± 0.7 (5.4)	1.2 ± 0.8 (1.9)	-4.9 ± 2.6 (6.6)
2021 October 21	12:52:10	509.036	2.080	173	1365	3898	1.170 ± 0.015	-0.097 ± 0.172	182 ± 19	3.5 ± 0.7 (5.4)	2.5 ± 0.8 (1.9)	-6.5 ± 2.6 (6.6)
2021 October 22	12:52:41	510.037	2.376	145	1282	3631	1.289 ± 0.017	0.047 ± 0.172	184 ± 19	-18.9 ± 0.7 (5.4)	-3.7 ± 0.8 (1.9)	-4.7 ± 2.6 (6.6)
2021 October 23	12:35:50	511.025	2.669	199	1614	5295	1.385 ± 0.014	-1.163 ± 0.131	226 ± 12	-8.8 ± 0.7 (5.4)	-1.0 ± 0.8 (1.9)	-2.9 ± 2.6 (6.6)
2021 October 24	13:17:42	512.054	2.975	154	1387	3813	1.256 ± 0.016	2.621 ± 0.165	47 ± 19	5.0 ± 0.7 (5.4)	6.0 ± 0.8 (1.9)	-2.9 ± 2.6 (6.6)
2021 October 25	08:44:44	512.864	3.215	194	1486	4517	1.255 ± 0.015	-1.313 ± 0.150	252 ± 16	1.1 ± 0.7 (5.4)	-2.9 ± 0.8 (1.9)	-6.3 ± 2.6 (6.6)
2021 October 26	11:57:48	513.998	3.551	199	1575	5157	1.402 ± 0.015	-1.607 ± 0.140	152 ± 13	-10.4 ± 0.7 (5.4)	-3.6 ± 0.8 (1.9)	-2.1 ± 2.6 (6.6)
2021 October 28	13:15:21	516.052	4.160	169	1455	4323	1.262 ± 0.016	-1.779 ± 0.164	228 ± 17	-2.0 ± 0.7 (5.4)	1.5 ± 0.8 (1.9)	-2.5 ± 2.6 (6.6)
2021 November 18	13:51:48	537.078	10.396	188	1618	4597	1.378 ± 0.014	-0.264 ± 0.133	176 ± 15	-7.9 ± 0.7 (5.4)	-1.1 ± 0.8 (1.9)	-0.0 ± 2.6 (6.6)
2021 November 19	12:16:07	538.011	10.672	210	1563	5203	1.393 ± 0.015	-2.637 ± 0.132	217 ± 12	-1.1 ± 0.7 (5.4)	-1.7 ± 0.8 (1.9)	-3.1 ± 2.6 (6.6)
2021 November 20	10:58:17	538.957	10.953	176	1611	4367	1.334 ± 0.014	2.960 ± 0.142	47 ± 16	4.8 ± 0.7 (5.4)	5.9 ± 0.8 (1.9)	-2.1 ± 2.6 (6.6)
2021 November 21	11:06:06	539.963	11.251	196	1590	4939	1.330 ± 0.014	-1.245 ± 0.140	230 ± 14	-2.5 ± 0.7 (5.4)	-3.4 ± 0.8 (1.9)	-3.4 ± 2.6 (6.6)
2021 November 22	11:39:43	540.986	11.555	200	1673	5173	1.467 ± 0.014	-1.392 ± 0.124	160 ± 13	-8.9 ± 0.7 (5.4)	-2.7 ± 0.8 (1.9)	-5.3 ± 2.6 (6.6)
2021 December 9	10:52:45	557.953	16.586	192	1618	4161	1.462 ± 0.014	-1.676 ± 0.130	168 ± 16	-3.0 ± 0.7 (5.4)	-0.2 ± 0.8 (1.9)	2.6 ± 2.6 (6.6)
2021 December 10	10:15:39	558.928	16.875	191	1603	4788	1.385 ± 0.014	2.357 ± 0.133	156 ± 14	4.1 ± 0.7 (5.4)	-0.2 ± 0.8 (1.9)	0.9 ± 2.6 (6.6)
2021 December 11	10:21:37	559.932	17.173	138	1441	3301	1.270 ± 0.015	-1.817 ± 0.159	217 ± 22	1.0 ± 0.7 (5.4)	-3.1 ± 0.8 (1.9)	-2.8 ± 2.6 (6.6)
2021 December 12	10:29:22	560.937	17.471	143	1613	3552	1.410 ± 0.014	-0.680 ± 0.133	104 ± 19	-1.5 ± 0.7 (5.4)	-1.7 ± 0.8 (1.9)	-1.4 ± 2.6 (6.6)
2021 December 14	13:25:28	563.059	18.101	158	1466	3620	1.281 ± 0.015	-0.254 ± 0.164	191 ± 20	2.7 ± 0.7 (5.4)	-1.6 ± 0.8 (1.9)	5.3 ± 2.6 (6.6)
2021 December 15	08:07:13	563.838	18.332	152	1497	3573	1.374 ± 0.015	-0.172 ± 0.145	223 ± 19	-1.9 ± 0.7 (5.4)	-6.3 ± 0.8 (1.9)	1.4 ± 2.6 (6.6)
2021 December 16	09:45:41	564.907	18.649	169	1623	4215	1.483 ± 0.014	-1.584 ± 0.128	200 ± 15	-3.0 ± 0.7 (5.4)	-0.8 ± 0.8 (1.9)	0.4 ± 2.6 (6.6)
2021 December 18	10:11:50	566.925	19.247	157	1114	3661	1.208 ± 0.018	-1.250 ± 0.202	231 ± 19	-3.1 ± 0.7 (5.4)	-6.7 ± 0.8 (1.9)	-0.3 ± 2.6 (6.6)
2022 January 6	10:01:22	585.918	24.880	213	1139	5683	1.463 ± 0.021	2.869 ± 0.191	136 ± 12	6.7 ± 0.7 (5.4)	3.8 ± 0.8 (1.9)	-2.3 ± 2.6 (6.6)
2022 January 8	09:41:27	587.904	25.469	197	1516	5119	1.386 ± 0.015	0.121 ± 0.142	144 ± 13	-2.4 ± 0.7 (5.4)	0.8 ± 0.8 (1.9)	3.8 ± 2.6 (6.6)
2022 January 9	09:43:21	588.905	25.766	203	1773	5150	1.478 ± 0.013	0.189 ± 0.111	236 ± 12	3.5 ± 0.7 (5.4)	0.6 ± 0.8 (1.9)	2.9 ± 2.6 (6.6)
2022 January 10	10:53:03	589.954	26.076	195	1630	4628	1.274 ± 0.014	0.133 ± 0.145	162 ± 16	-1.0 ± 0.7 (5.4)	5.6 ± 0.8 (1.9)	2.2 ± 2.6 (6.6)
2022 January 11	06:00:12	590.750	26.313	209	1740	5399	1.423 ± 0.013	-0.220 ± 0.130	211 ± 13	-3.8 ± 0.7 (5.4)	-3.7 ± 0.8 (1.9)	-4.3 ± 2.6 (6.6)
2022 January 12	10:19:13	591.930	26.663	205	1588	5029	1.474 ± 0.015	-1.348 ± 0.128	206 ± 13	-1.3 ± 0.7 (5.4)	-0.2 ± 0.8 (1.9)	3.0 ± 2.6 (6.6)
2022 January 13	09:46:35	592.907	26.952	195	919	5014	0.846 ± 0.016	3.462 ± 0.245	86 ± 14	-0.3 ± 0.7 (5.4)	3.4 ± 0.8 (1.9)	13.7 ± 2.6 (6.6)
2022 January 15	10:15:20	594.927	27.551	207	1502	5161	1.419 ± 0.015	-0.718 ± 0.151	137 ± 13	2.8 ± 0.7 (5.4)	1.2 ± 0.8 (1.9)	4.9 ± 2.6 (6.6)
2022 January 18	09:43:56	597.906	28.435	205	1100	4909	0.999 ± 0.015	0.500 ± 0.195	152 ± 14	4.1 ± 0.7 (5.4)	-0.4 ± 0.8 (1.9)	12.1 ± 2.6 (6.6)
2022 January 19	09:08:20	598.881	28.724	208	1282	5238	1.267 ± 0.015	-0.503 ± 0.156	254 ± 12	3.0 ± 0.7 (5.4)	-1.2 ± 0.8 (1.9)	6.1 ± 2.6 (6.6)
2022 January 20	08:50:05	599.868	29.017	199	641	5342	1.209 ± 0.037	0.740 ± 0.368	75 ± 14	-0.7 ± 0.7 (5.4)	5.1 ± 0.8 (1.9)	12.3 ± 2.6 (6.6)
2022 January 21	08:56:25	600.873	29.315	205	1041	4678	0.952 ± 0.015	0.265 ± 0.225	182 ± 15	0.4 ± 0.7 (5.4)	-2.6 ± 0.8 (1.9)	8.6 ± 2.6 (6.6)
2022 January 22	08:02:07	601.835	29.600	130	1235	2938	1.451 ± 0.019	-1.185 ± 0.159	177 ± 22	1.1 ± 0.7 (5.4)	2.4 ± 0.8 (1.9)	3.2 ± 2.6 (6.6)
2022 January 24	09:09:48	603.882	30.207	196	682	5684	1.306 ± 0.036	-1.913 ± 0.336	200 ± 13	15.8 ± 0.7 (5.4)	0.5 ± 0.8 (1.9)	9.0 ± 2.6 (6.6)
2022 January 25	09:17:16	604.887	30.505	169	1032	4177	1.462 ± 0.023	-0.432 ± 0.212	117 ± 16	2.1 ± 0.7 (5.4)	4.3 ± 0.8 (1.9)	5.4 ± 2.6 (6.6)
2022 January 28	08:31:31	607.855	31.385	172	1220	3723	1.509 ± 0.020	-0.355 ± 0.183	200 ± 18	-1.6 ± 0.7 (5.4)	-0.1 ± 0.8 (1.9)	0.7 ± 2.6 (6.6)
2022 January 30	08:28:11	609.853	31.978	182	576	3962	1.116 ± 0.038	0.963 ± 0.418	102 ± 18	3.9 ± 0.7 (5.4)	3.7 ± 0.8 (1.9)	27.1 ± 2.6 (6.6)

2.2 Photometric observations

2.2.1 TESS light curve

LkCa 4 (TIC 58108662) was also observed by TESS (Ricker et al. 2014), with a cadence of 2 min, during the monitoring of Sectors 43 (2021 Sep 16 – Oct 12) and 44 (2021 Oct 12 – Nov 06) over a total time span of 49 d. The second monitoring was contemporaneous with SPIRou observations, although both instruments are sensitive to different wavelengths (the TESS filter being centred close to the mean wavelength of the I_c band).

The TESS data were processed by the Science Processing Operations Center (SPOC; Jenkins et al. 2016) data pipeline (version 5.0). For each sector, the observations were stopped for about 1 d between two physical orbits of the telescope to download the data, yielding a total of about 46 d of science observations¹. As we want to use these data to characterise stellar variability, we kept the Pre-search Data Conditioning Single Aperture Photometry (PDCSAP) flux, already corrected for instrumental variations and contamination from nearby stars (Smith et al. 2012; Stumpe et al. 2012, 2014), that was not flagged by the SPOC pipeline.

We filtered the light curves from flares by applying the same 3σ -clipping process involving Gaussian Process Regression (GPR;

Rasmussen & Williams 2006) as in Finocietty et al. (2021). The obtained filtered light curve (see Fig. 1) was then modelled using a Gaussian Process (GP) with a quasi-periodic kernel (Eq. (1)) known to be adapted for the description of signals induced by stellar activity (Rajpaul et al. 2015) :

$$k(t, t') = \theta_1^2 \exp \left[-\frac{(t - t')^2}{2\theta_2^2} - \frac{\sin^2 \left(\frac{(t - t')\pi}{\theta_3} \right)}{2\theta_4^2} \right] \quad (1)$$

where t and t' are the dates associated with two different observations. θ_1 corresponds to the amplitude of the GP, θ_2 represents the exponential decay time-scale (giving an estimate of the typical spot lifetime), θ_3 is the recurrence time-scale (expected to be equal, or very close, to the stellar rotation period) and θ_4 is the smoothing parameter controlling the short-term variations that are included in the fit.

We find that the decay time-scale is equal to 150 ± 37 d, indicating that the light curve is very close to a purely periodic signal over the time interval covered by the TESS data (i.e. the spot distribution does not evolve much over the time span of the TESS observations). We also estimate $\theta_3 = 3.372 \pm 0.002$ d, thus consistent with the stellar rotation period of 3.374 d previously reported by Grankin et al. (2008) and $\theta_4 = 0.612 \pm 0.096$. We see a vertical jump in the light curve between Sectors 43 and 44 (BJD \approx 2459500), likely due to instrumental effects. As part of the process, we therefore derived the best constant mean value of each Sector to model the

¹ Details on the processing of the data can be found in the Data Release notes of Sector 43 and 44 (DR62 and DR64) available at https://archive.stsci.edu/tess/tess_drn.html.

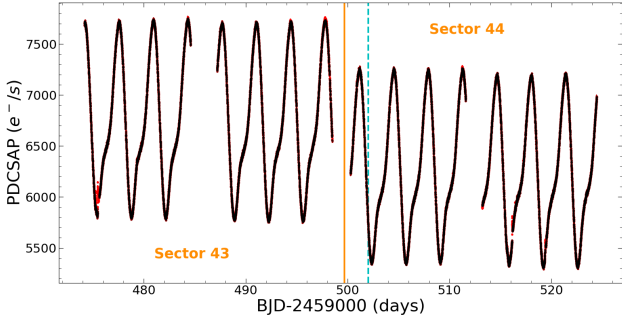


Figure 1. TESS Pre-search Data Conditioning Single Aperture Photometry. The black dots correspond to the filtered light curve while the red ones are those that were either rejected by our 3σ -clipping process or flagged by the SPOC pipeline. The cyan dashed vertical line denotes the start of the SPIRou monitoring while the orange vertical line delimits the light curve of Sector 43 from that of Sector 44.

flux with the GP, found to be equal to $m_1 = 6584 \pm 417 \text{ e}^-/\text{s}$ and $m_2 = 6154 \pm 417 \text{ e}^-/\text{s}$ for Sector 43 and 44, respectively. We also notice a vertical shift between the first and second half of the TESS light curve associated with Sector 44 (around $\text{BJD} = 2459515$), that we corrected (by increasing the lower section) to ensure that both parts of the curve have the same mean level.

We used the stellar rotation period derived from our filtered TESS light curve to compute the rotational cycles c according to:

$$\text{BJD (d)} = 2459502.02 + 3.372 c \quad (2)$$

where the initial date ($\text{BJD}_0 = 2459502.02$) was arbitrarily chosen to correspond to the date of our first SPIRou observation of LkCa 4.

The TESS monitoring of Sector 44 being contemporaneous with SPIRou observations, we also computed relative photometry (with respect to the mean value m_2 derived through GPR) and median time every 20 points, resulting in 741 photometric data points to be included in the imaging process, for which we set the uncertainty to 2.4 mmag (see Sec. 3), i.e. equal to the RMS dispersion of the selected TESS data about the GPR fit, and slightly larger than the nominal error bar of the TESS data, of 1.9 mmag.

2.2.2 Ground-based observations

Fourteen additional photometric observations were collected in the V , R_j , R_c , I_j and I_c bands with the ground-based CrAO 1.25-m AZT-11 telescope from 2021 Oct 10 to 2022 Jan 27. The full log of these observations can be found in Table A1.

These measurements also show a brightness modulation, that can be fitted with a periodic function (sine wave plus two harmonics) as shown in Fig. 2, assuming the stellar rotation period derived from the TESS light curve. As no nominal uncertainties are available, we estimated empirical error bars by setting them to ensure a unit reduced chi-squared (χ_r^2) between the measurements and the model. Using only the magnitudes in the V , R_c and I_c bands, we found typical uncertainties of 16, 9 and 6 mmag, for each band respectively. As expected, we see that the amplitude of the light curve decreases with wavelength and is equal to 0.464 ± 0.020 , 0.447 ± 0.011 and 0.323 ± 0.008 mag in the V , R_c and I_c bands, the latter being consistent with the TESS light curve featuring a full amplitude of 0.3207 ± 0.0006 mag. The observed photometric modulation clearly reflects the presence of large surface inhomogeneities coming in and going out of the observer’s view as the star rotates.

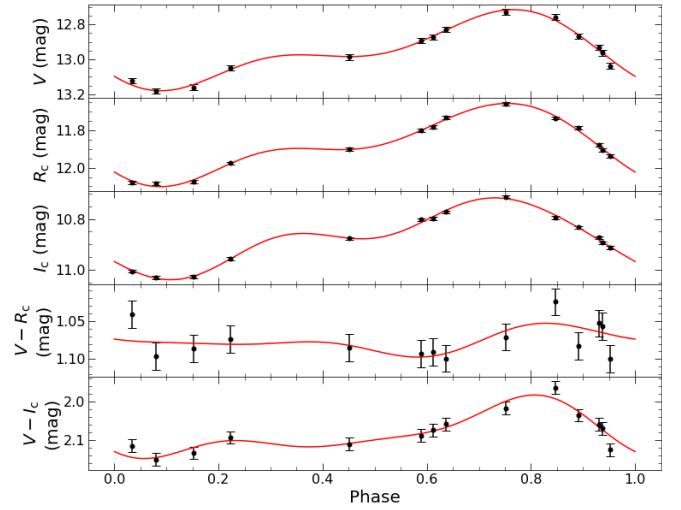


Figure 2. Magnitudes in the V , R_c , I_c bands (1st to 3rd panels) and $V - R_c$ and $V - I_c$ colour indexes (4th and 5th panels) collected with the ground-based AZT-11 telescope at the CrAO between 2021 October and 2022 January. For the three first panels, the red line corresponds to a fit to the data involving a sine wave and the first two harmonics. The empirical error bars on the magnitudes are then set to ensure a unit χ_r^2 between the data and these models (16, 9 and 6 mmag for the V , R_c and I_c bands, respectively). For the last two panels, the red curves depict the difference between the previous models. All light curves are phased using the ephemeris of Sec. 2.2.1.

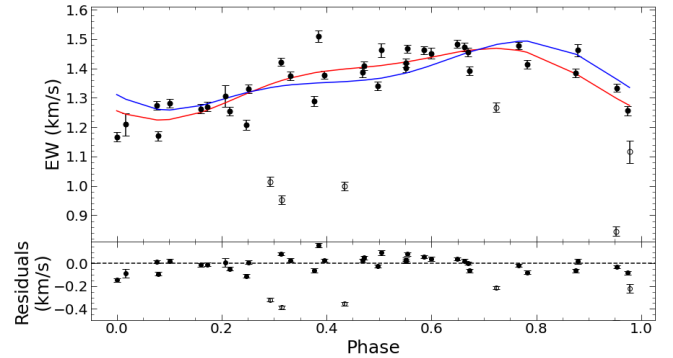


Figure 3. Phase-folded EWs of the Stokes I LSD profiles. *Top panel:* The measurements along with their error bars are shown as black dots. The ZDI fit is displayed as a blue line while the red curve corresponds to a periodic fit (including the fundamental and the first harmonic) to the measurements associated with a full circle (the open circles being rejected through a σ -clipping process). Both models show a full amplitude of $\sim 0.25 \text{ km s}^{-1}$, corresponding to a peak-to-peak variation of 20%. *Bottom panel:* Residuals between the measurements and the ZDI fit, with a RMS dispersion of 0.06 km s^{-1} (when excluding the open circles).

3 TOMOGRAPHIC IMAGING

ZDI (Semel 1989; Brown et al. 1991; Donati & Brown 1997; Donati et al. 2006, 2014) is an efficient tomographic technique inspired from medical applications allowing one to recover the brightness distribution and large-scale magnetic topology at the surface of an active star. We applied this technique on both our sets of Stokes I and Stokes V LSD profiles to recover brightness and magnetic maps of LkCa 4.

ZDI is an iterative process based on the principles of maximum entropy that iteratively inverts sets of Stokes I and V LSD profiles,

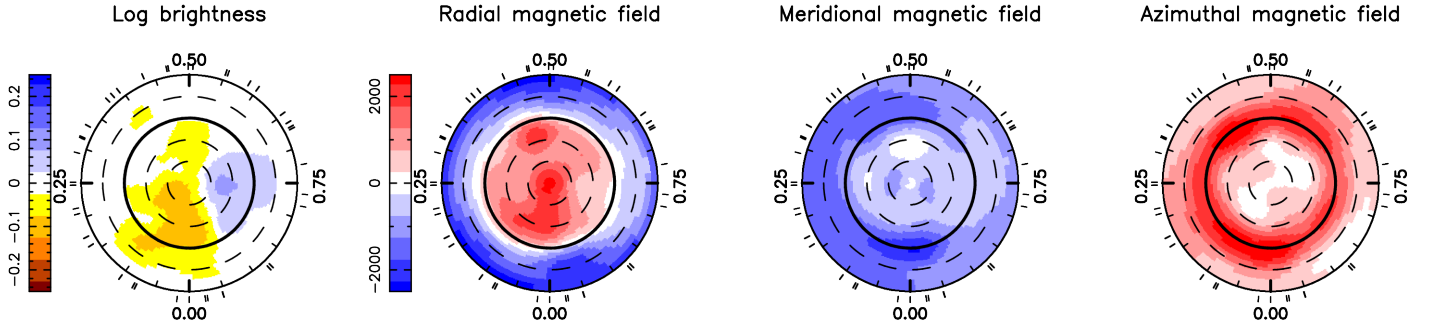


Figure 4. ZDI maps of the logarithmic brightness surface (left panel), radial, meridional and azimuthal magnetic field components (second to fourth panels). The star is shown in a flattened polar view, with the pole at the center, the equator as a bold circle and the 30° and 60° latitude parallels depicted in dashed circles. The star is shown down to -60° below which almost nothing contributes to the data. For the brightness map, yellow/brown corresponds to dark spots while blue corresponds to warm plages. For the magnetic maps, red is associated to a radial, meridional and azimuthal field pointing outwards, polewards and counter-clockwise, respectively. The ticks around the star refer to the phases of the 41 spectropolarimetric observations collected with *SPIRou*.

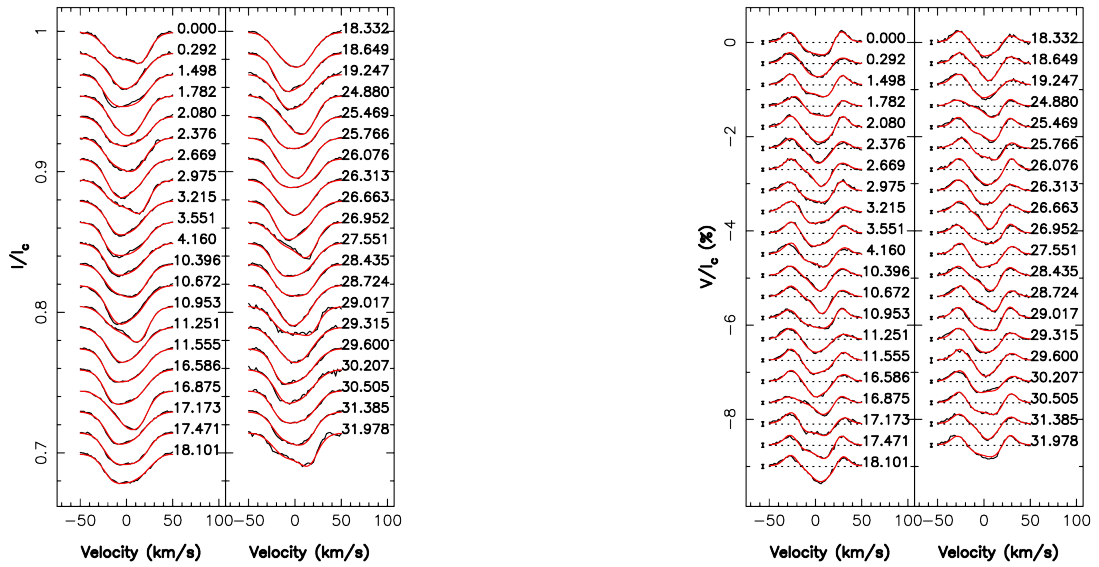


Figure 5. Stokes I (left) and V (right) LSD profiles. For both panels, the observed Stokes profiles are shown in black while the ZDI fit is depicted as a red line. The rotation cycle associated with each observation is mentioned on the right of each profile. For Stokes V LSD profiles, we also display the 3σ error bars on the left of each profile.

by adding brightness inhomogeneities and magnetic regions at the surface of the star and comparing the associated LSD profiles with the observed ones until reaching a unit χ_r^2 . In practice, the stellar surface is divided in 3000 cells; we then compute the local Stokes I and V LSD profiles from each cell using the Unno-Rachkovsky’s solution of the polarized radiative transfer equations in a plane-parallel Milne-Eddington atmosphere (e.g. Landi Degl’Innocenti & Landolfi 2004). The built-in prescription for the limb-darkening variations has been replaced by a linear law for the continuum only associated with a coefficient $\epsilon = 0.3$, consistent with $T_{\text{eff}} = 4100$ K and $\log g = 4.0$ (Claret & Bloemen 2011). The synthetic LSD profiles are then derived by integrating all local profiles over the visible stellar hemisphere.

The relative brightness is simply described as a set of independent values for each grid cell at the surface of the star; the large-scale magnetic field is expressed as the sum of a poloidal and a toroidal component, both described as spherical harmonic expansions (Donati et al. 2006; Finocciety & Donati 2022).

As the equivalent width (EW) of our Stokes I LSD profiles is found to be modulated with rotation phase (by about 20% peak-to-peak, see

Fig. 3), we added an empirical description of how the local profile varies with temperature. In practice, we simply assume that the depth of the local profile varies as a power δ of the local brightness (over the limited range of brightness values that we reconstruct, see Sec. 3.1). Since the EWs of Stokes I profiles are smaller when the star is fainter, it already indicates that δ is positive.

Given the small amount of surface differential rotation reported for LkCa 4 (Donati et al. 2014), we will first consider that the star rotates as a solid body before estimating the differential rotation parameters using our data in Sec 3.2.

We fitted our LSD profiles using a line model featuring a mean wavelength, Doppler width and Landé factor of 1750 nm, 3.4 km s^{-1} and 1.2, respectively. We set the inclination $i = 70^\circ$ and line-of-sight projected equatorial velocity $v \sin i = 28 \text{ km s}^{-1}$ as in Donati et al. (2014). As part of the imaging process, we also retrieve a bulk radial velocity of $16.9 \pm 0.1 \text{ km s}^{-1}$, consistent with the value reported in Donati et al. (2014). Table 2 gathers all physical parameters of LkCa 4.

Table 2. Physical parameters of LkCa 4. From top to bottom: distance from Earth, bulk radial velocity, effective temperature, rotation period, luminosity, inclination, line-of-sight projected equatorial velocity, minimal stellar radius, stellar radius, stellar mass, logarithmic surface gravity, rotation rate at the equator, pole-to-equator rotation rate difference and age.

Parameter	Value	Reference
d (pc)	129.8 ± 0.3	Gaia Collaboration et al. (2021)
Bulk RV (km s ⁻¹)	16.9 ± 0.8	This work (Sec. 3)
T_{eff} (K)	4100 ± 50	Donati et al. (2014)
P_{rot} (d)	3.372 ± 0.002	This work (Secs. 2.2.1 & 4)
$\log L_*/L_{\odot}$	-0.04 ± 0.11	Donati et al. (2014)
i (°)	70	Donati et al. (2014)
$v \sin i$ (km s ⁻¹)	28.0 ± 0.5	Donati et al. (2014)
$R_* \sin i$ (R _⊙)	1.87 ± 0.03	Donati et al. (2014)
R_* (R _⊙)	2.0 ± 0.2	Donati et al. (2014)
M_* (M _⊙)	0.73 ± 0.05	This work
$\log g$ (cgs units)	3.8 ± 0.1	Donati et al. (2014)
Ω_{eq} (mrad d ⁻¹)	1864.0 ± 0.2	This work (Sec. 3.2)
dΩ (mrad d ⁻¹)	5.8 ± 0.8	This work (Sec. 3.2)
Age (Myr)	~1.3	This work

3.1 Brightness and magnetic imaging

In this Section, we assume that the star rotates as a solid body. We first simultaneously inverted both our Stokes I and V LSD profiles using ZDI without including the TESS data in the fitting process. Both sets of LSD profiles were adjusted down to $\chi_r^2 = 1$. We show the reconstructed brightness and magnetic maps in Fig. 4 with the associated profiles in Fig. 5. At this stage, adjusting δ , so that the modulation with rotation phase of the EW of the synthetic LSD profiles matched observations, was essential, which yielded $\delta = 1.0 \pm 0.1$. This ensures at the same time that the amplitude of the predicted light curve is consistent with that observed with TESS and at CrAO (once the reconstructed brightness image in the H band is translated into an I_c band image using the Planck function, assuming a photospheric temperature of 4100 K).

We note that the brightness distribution is mainly characterized by two large structures covering about 7% of the stellar surface: a dark spot at phase 0.1 spreads between the pole and the equator whereas a bright plage is reconstructed at phase 0.75. These features are the ones that generate most of the observed rotational modulation of both the light curve and the EWs of LSD Stokes I profiles. The reconstructed spot coverage is much lower than that derived by Gully-Santiago et al. (2017), reaching up to 80%, which implies that the star is most likely evenly covered with small-scale cool spots that are not resolved by ZDI.

In a second step, we reconstructed the brightness distribution and large-scale magnetic topology from the Stokes I and V LSD profiles and the 741 additional photometric data points, proceeding as described in Finociety et al. (2021) to take into account (with the Planck function) that the spectropolarimetric and photometric data have different average wavelengths. Both spectroscopic and photometric data were fitted down to a unit χ_r^2 . We find that the spot coverage is increased up to 9% and the reconstructed map features more low-latitude structures and enhanced contrasts between the reconstructed spots and the quiet photosphere (top panel of Fig. 6). We however see no major differences in the location of the reconstructed brightness features. The residuals in the fitted light curve show low-amplitude structures that were not fitted (bottom panel of Fig. 6), likely due to, rapidly evolving, surface features. Adding the TESS data in the fitting process does not change the magnetic maps

as the photometry mainly informs on the contrast of the brightness features.

The magnetic topology is rather simple and similar to that obtained by Donati et al. (2014) from optical data. The average magnetic strength is equal to ~1.9 kG but can be locally more intense due to a strong radial field reaching up to ~2.3 kG. The poloidal component of the magnetic field, enclosing ~65% of the overall reconstructed magnetic energy, mainly consists of a strong and axisymmetric dipole (~2.2 kG) slightly tilted with respect to the rotation axis by 3° towards phase 0.31, concentrating about 85% of the poloidal energy. The toroidal component is also mainly axisymmetric and characterized by a strong azimuthal field ring (~1.4 kG) encircling the star close to the equator. We also note that the regions associated with the strongest radial field coincide more or less with the largest cool spot.

In order to investigate whether the strength of the local magnetic field may also partly explain the variations of the EW of the Stokes I LSD profiles, we attempted to reconstruct the brightness and large-scale magnetic field of LkCa 4 using the filling factors f_I and f_V describing the fraction of the grid cells covered by small- and large-scale magnetic fields and respectively affecting Stokes I and Stokes V profiles, as defined in Morin et al. (2008). More specifically, B/f_V is the local strength of the magnetic field, f_V the fraction of the cells contributing to the large-scale field, and f_I the fraction of the cells contributing to the small-scale field. Whereas we set $f_V = f_I = 1$ for the previous reconstructions², we now assume $f_V = 0.5$ and $f_I = 1$, i.e., the local field is twice as strong as before, with only half of the cells contributing to the large-scale field and the whole cells to the small scale field. With these assumptions, we empirically find $\delta = 0.9$ (compatible with the previous estimate), indicating that the observed variations of EW are indeed mostly due to the temperature of surface features and only slightly to the magnetic field. Besides, the reconstructed brightness and magnetic maps are globally consistent with the ones shown in Fig. 4, with slightly less contrasted brightness features and a slightly weaker magnetic field.

We computed the longitudinal field B_ℓ as the first moment of the Stokes V LSD profiles (Donati et al. 1997). We find that B_ℓ ranges from ~50 to ~250 G with uncertainties ranging from 12 to 23 G (median of 15 G). The B_ℓ measurements show a clear modulation and can be fitted down to the noise level with a periodic signal (sine + 2 harmonics) as no significant evolution is seen in these data (Fig. 7). This fit provides a stellar rotation period of 3.373 ± 0.001 d, consistent with TESS photometric variations (3.372 ± 0.002 d) and with the value provided when using a quasi-periodic GP to model the longitudinal field (3.373 ± 0.002 d).

3.2 Surface differential rotation

Our data are spread over 32 rotation cycles, during which the brightness map and the large-scale magnetic topology have potentially evolved under the effect of differential rotation, although the expected level of differential rotation is weak (Donati et al. 2014). ZDI allows one to take into account this variability assuming that the rotation rate at the surface of the star follows a solar-like law given by :

$$\Omega(\theta) = \Omega_{\text{eq}} - (\cos \theta)^2 d\Omega \quad (3)$$

² Line broadening being dominated by rotation, magnetic broadening has a minor impact on the Stokes I LSD profiles, hence our initial assumption on the f_I and f_V filling factors.

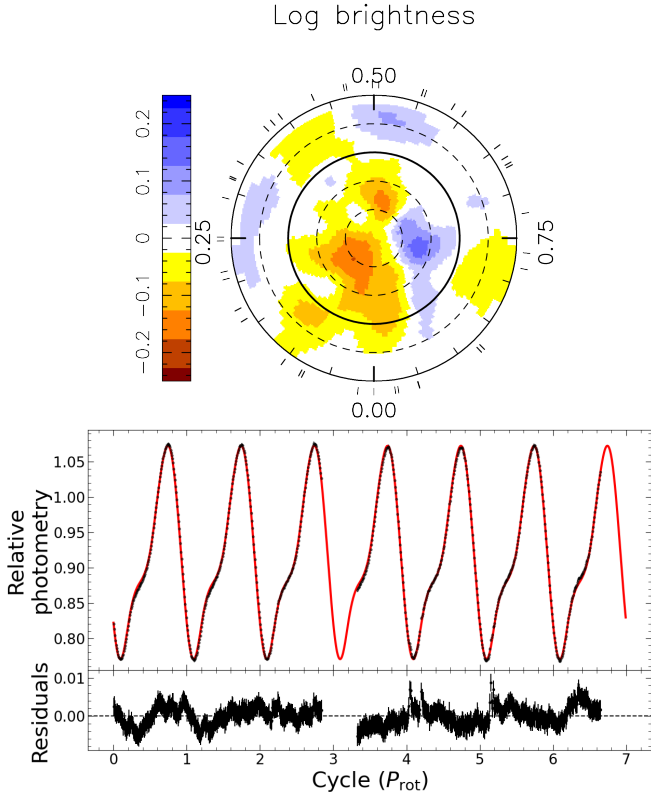


Figure 6. ZDI reconstruction using *SPIRou* and *TESS* data simultaneously. *Top panel:* Map of the logarithmic relative brightness as described in Fig. 4. *Bottom panel:* Fit of the light curve. In the first plot, we show the 741 relative photometry values from *TESS* data in black and the ZDI fit in red. The second plot displays the residuals between the data and the fit, exhibiting a RMS dispersion of 2.4 mmag.

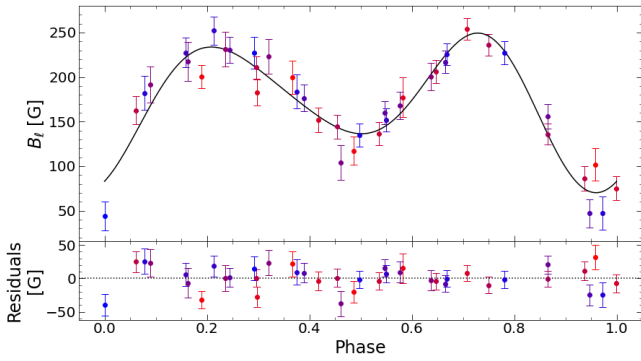


Figure 7. Phase-folded longitudinal field of *LkCa 4*. *Top panel:* the measurements are displayed as coloured dots while the periodic fit is shown in solid black line. *Bottom panel:* Residuals between the measurements and the model, exhibiting a RMS dispersion of 17 G corresponding to $\chi_r^2 = 1.14$. In both panels symbol colour depicts time, ranging from blue to red from the beginning to the end of our observations.

where θ is the colatitude, Ω_{eq} and $d\Omega$ the parameters of the differential rotation law, characterizing the rotation rate at the equator and the pole-to-equator rotation rate difference, respectively.

In practice, we set the amount of information that ZDI is allowed to reconstruct and we look for the DR parameters that minimize χ_r^2 . Fitting Stokes *I* and *V* profiles independently yields χ_r^2 maps from

which we derive optimal parameters and their error bars (Donati et al. 2003; see Fig. 8). From the brightness map we derive $\Omega_{\text{eq}} = 1864.6 \pm 0.8 \text{ mrad d}^{-1}$ and $d\Omega = 5.5 \pm 2.6 \text{ mrad d}^{-1}$ (implying a period of 3.3697 ± 0.0014 and 3.3797 ± 0.0049 d at the equator and at the pole, respectively). The magnetic maps yield fully compatible but more accurate values, with error bars more than $3\times$ smaller. We find $\Omega_{\text{eq}} = 1864.0 \pm 0.2 \text{ mrad d}^{-1}$ and $d\Omega = 5.8 \pm 0.8 \text{ mrad d}^{-1}$ (corresponding to a period of 3.3708 ± 0.0004 and 3.3813 ± 0.0015 d at the equator and at the pole, respectively). The slope of the major axis of the confidence ellipse provides an estimate of the colatitude associated with the barycentre of the brightness or magnetic distribution, found to be equal to $\sim 55^\circ$ and $\sim 60^\circ$. These results indicate that both brightness and magnetic regions are, in average, located at similar latitudes, explaining why the longitudinal field, the photometry and the RVs (Section 4) yield similar values for the stellar rotation period.

The estimates of differential rotation inferred from the Stokes *I* LSD profiles are sensitive to the value of δ . Varying δ within the error bars (i.e. between 0.9 and 1.1) nevertheless yields estimates of $d\Omega$ that are still compatible with the value reported above within 1σ .

We chose a unique set of parameters to described the DR at the surface of *LkCa 4*, taken as the weighted means of both estimates: $\Omega_{\text{eq}} = 1864.0 \pm 0.2 \text{ mrad d}^{-1}$ and $d\Omega = 5.8 \pm 0.8 \text{ mrad d}^{-1}$. These weighted means actually yield the same values as those derived from our Stokes *V* LSD profiles since they are more accurate than those provided by our Stokes *I* profiles. This implies that the rotation period ranges from 3.3708 ± 0.0004 d at the equator to 3.3813 ± 0.0015 d at the pole. The surface DR of *LkCa 4* is thus $10\times$ weaker than that of the Sun and significantly different from 0 at a 7σ level.

4 FILTERING THE ACTIVITY JITTER

To investigate the impact of activity on the RV curve (activity jitter), we computed the RV of the star corresponding to each spectropolarimetric observation as the first moment of the Stokes *I* LSD profiles (e.g. Donati et al. 2017; Yu et al. 2019; Finocietty et al. 2021). We estimated the associated photon-noise uncertainties from the dispersion of the RV measurements on simulated noisy profiles (from the synthetic set of profiles provided by ZDI) featuring the same SNR as the observed ones for several realisations of noise. The computed error bars are typically equal to 0.15 km s^{-1} , thus $2.5\times$ larger than those obtained from *ESPaDOnS* data (Donati et al. 2014). Such a difference is most likely related to the depth of the spectral lines, about $3.5\times$ shallower in the infrared than in the optical. The measured RVs exhibit a RMS dispersion of 1.45 km s^{-1} with a $\chi_r^2 = 84.89$, with respect to a model with constant RV.

We computed the RVs associated with the synthetic Stokes *I* profiles provided by the reconstructed brightness maps obtained with ZDI. Comparing these values with the raw measurements, we see that the RVs are fitted down to $\chi_r^2 = 6.56$ when applying ZDI to *SPIRou* data alone and down to $\chi_r^2 = 7.35$ when ZDI is applied to *SPIRou* and *TESS* data simultaneously. The corresponding RMS dispersion of the filtered RVs (i.e. the difference between the observed and modeled RVs) is equal to 0.45 km s^{-1} and 0.48 km s^{-1} , showing that adding photometry in our process only slightly degrades our jitter filtering efficiency (see Fig. 9).

We also used a GP with the quasi-periodic kernel introduced in Sec 2.2.1. The log likelihood function we maximize (Eq. (4)) takes

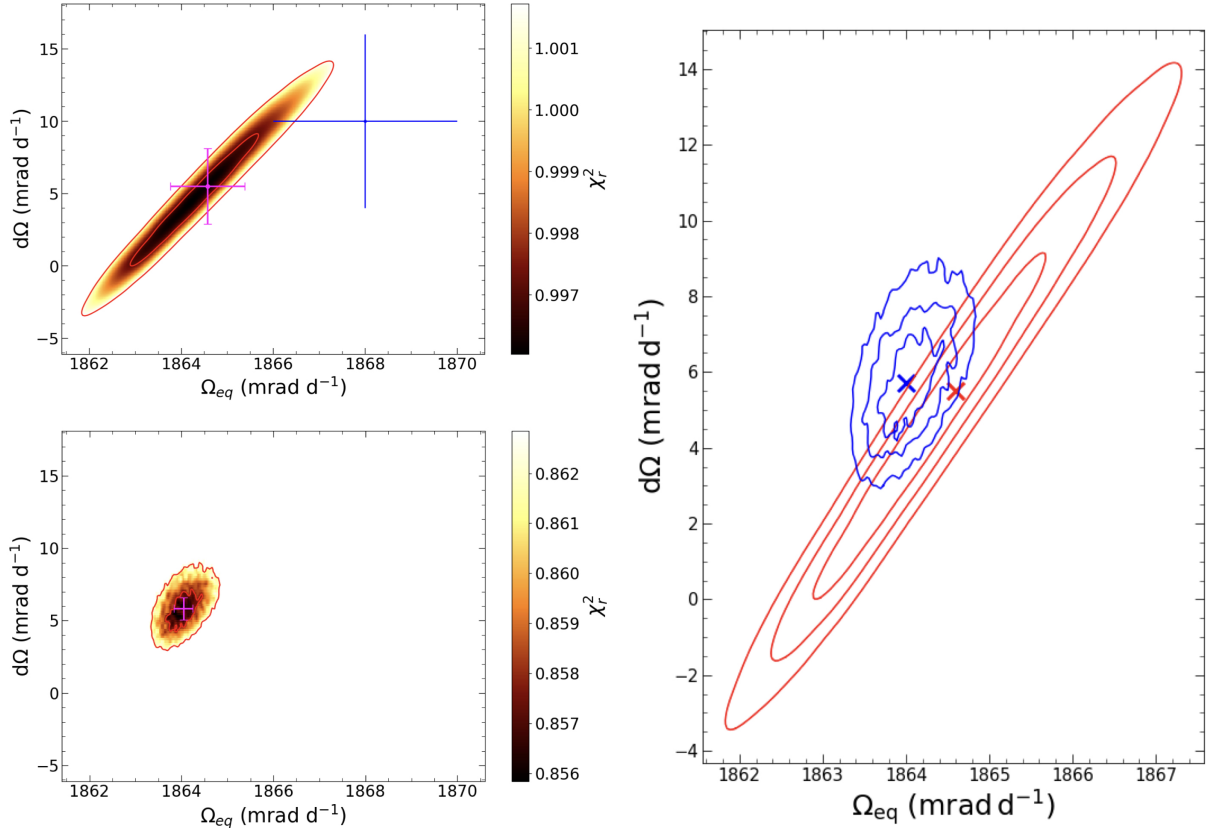


Figure 8. Differential rotation at the surface of LkCa 4 as measured from SPIRou data. *Left panels:* χ_r^2 maps in the $\{\Omega_{\text{eq}}, d\Omega\}$ space obtained from Stokes I (top) and V (bottom) LSD profiles, with Ω_{eq} and $d\Omega$ being the rotation rate at the equator and the difference of rotation rate between the pole and the equator, respectively. Red ellipses show the contours of 68% (1σ) and 99.7% (3σ) confidence levels for both parameters as a pair. The magenta cross depicts our optimal value with its associated error bars derived from a paraboloid fit to the χ_r^2 map, while the blue one in the top plot corresponds to the estimate reported by [Donati et al. \(2014\)](#) from optical data. *Right panel:* Comparison of the contours associated with the 1σ , 2σ and 3σ confidence levels obtained from Stokes I (red) and V (blue) LSD profiles. The coloured crosses depicts the optimal values derived with SPIRou data.

into account an additional term corresponding to an excess of uncorrelated noise s as in [Finociety et al. \(2021\)](#).

$$\log \mathcal{L} = -\frac{1}{2} \left(N_0 \log 2\pi + \log |\mathbf{K} + \mathbf{\Sigma} + \mathbf{S}| + \mathbf{y}^T (\mathbf{K} + \mathbf{\Sigma} + \mathbf{S})^{-1} \mathbf{y} \right) \quad (4)$$

where N_0 refers to the number of measured RVs, \mathbf{K} is the covariance matrix associated to the quasi-periodic kernel, $\mathbf{\Sigma}$ is the diagonal matrix containing the squared error bars on the measurements, $\mathbf{S} = s^2 \mathbf{I}$ with \mathbf{I} being the identity matrix and \mathbf{y} is the vector gathering the measured RVs.

We sampled the posterior distributions of all the parameters (i.e. the amplitude of the GP θ_1 , the exponential decay timescale θ_2 , the rotation period θ_3 , the smoothing parameter θ_4 and the excess of uncorrelated noise s) with a Monte Carlo Markov Chain (MCMC) approach using the `EMCEE PYTHON` module ([Foreman-Mackey et al. 2013](#)). More specifically, we ran our MCMC on 5000 iterations of 100 walkers and then removed a burn-in period of 500 iterations before estimating the best value of each parameter, chosen to be the median of the posterior distributions.

The optimal GP parameters are listed in [Table 3](#) whereas the best fit is shown in [Fig 9](#). GPR yields a 15% lower dispersion of the filtered RVs with respect to ZDI of 0.38 km s^{-1} associated with a $\chi_r^2 = 4.20$. In any case, the dispersion of the filtered RVs is 2.5–3 times larger than the typical measured error bars (0.15 km s^{-1}).

Table 3. Best value for the parameters involved in the GPR derived from the MCMC approach. We list the hyperparameters in the first column, the priors used in the MCMC in the second column (with the lower and upper limits of the interval) and the best estimate (taken as the median of the posterior distribution) in the last column.

Hyperparameter	Prior	Estimate
θ_1 [km s^{-1}]	Uniform (0, 10)	1.87 ± 0.86
θ_2 [d]	Uniform (0, 400)	262 ± 85
θ_3 [d]	Uniform (3, 4)	3.372 ± 0.002
θ_4	Uniform (0, 1)	0.50 ± 0.14
s [km s^{-1}]	Uniform (0, 1)	0.37 ± 0.06

From our MCMC, we note that $s = 0.37 \pm 0.06 \text{ km s}^{-1}$ is not compatible with 0, reflecting that our error bars are apparently underestimated, probably as a result of intrinsic variability induced by activity. In addition, the exponential decay-time scale is not well constrained (see corner plot in [Fig. 10](#)) indicating that the rotationally modulated component of the activity signal remains stable over the time span of our observations, despite some dispersion observed at the end of the SPIRou campaign (most likely due to bad weather conditions in 2022 January). The stellar rotation period derived from

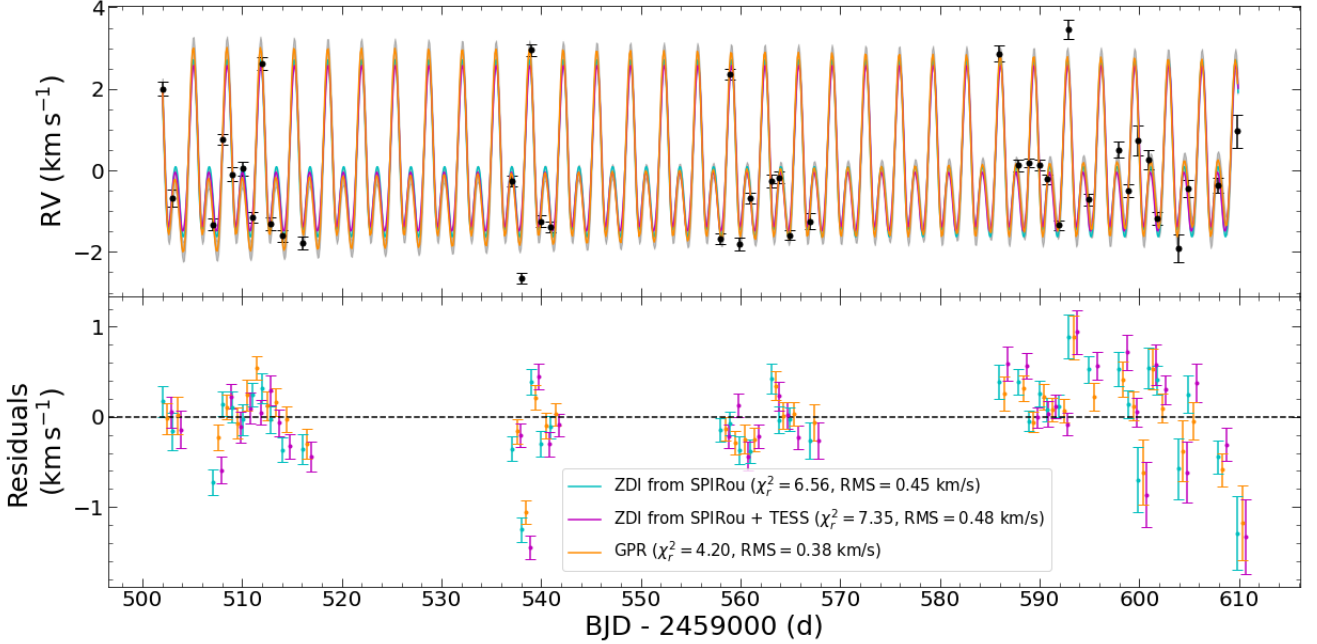


Figure 9. RVs of LkCa 4 measured from *SPIRou* data. *Top panel:* The raw observed RVs are shown as black dots with their associated error bars. They exhibit a full amplitude of 6.10 km s^{-1} and a RMS dispersion of 1.46 km s^{-1} . The cyan and magenta curves correspond to models derived from the ZDI reconstruction taking into account *SPIRou* data alone or *SPIRou* and *TESS* data simultaneously, respectively. The orange curve represents the GPR with the 1σ confidence area in light grey. *Bottom panel:* Filtered RVs associated to each of the 3 models, with the same colour code as in the top panel. We obtained RMS dispersions of the filtered RVs of 0.45 , 0.48 and 0.38 km s^{-1} , for cyan, magenta and orange models, respectively. We slightly shift the filtered RVs along the horizontal axis for each model for clarity purposes.

these RVs is also equal to 3.372 ± 0.002 , again consistent with those inferred from *TESS* data and B_ℓ measurements.

We computed the Generalised Lomb-Scargle Periodogram (Zechmeister & Kürster 2009) using the `PYASTRONOMY PYTHON` module (Czesla et al. 2019) of the raw and filtered RVs obtained with the three models (see Fig. 11). We do not see any significant peak in these periodograms, indicating that our data do not provide any evidence for a hJ orbiting LkCa 4. In order to investigate the upper mass limit of a potential planet that can be detected from our data, we proceeded as in Yu et al. (2019) and Finocietty et al. (2021). We first simulated RV curves including the RV activity jitter (using the derived GPR) and a planetary signature (assuming a circular orbit for various masses and distances from the host star). For each curve, we collected 41 measurements following the same temporal sampling as our actual *SPIRou* data, for which we added a white noise of 0.400 km s^{-1} (i.e. taking into account the photon-noise uncertainty of our observations and the uncorrelated noise derived from our GPR). We then fitted the simulated datasets using (i) a model including the activity jitter only and (ii) a model including both contributions of the activity jitter and the planet. We assume that a planet is reliably detected (i.e. at a $> 3\sigma$ level) when the difference in logarithmic marginal likelihood is larger than 10 (e.g. Yu et al. 2019; Finocietty et al. 2021). From these simulations, we find that we can safely claim that a planet is detected only if the semi-amplitude of the induced RV signal is larger than 0.44 km s^{-1} , which corresponds to a $4.3 M_{\text{Jup}}$ planet at 0.1 au (i.e. $P = 13 \text{ d}$).

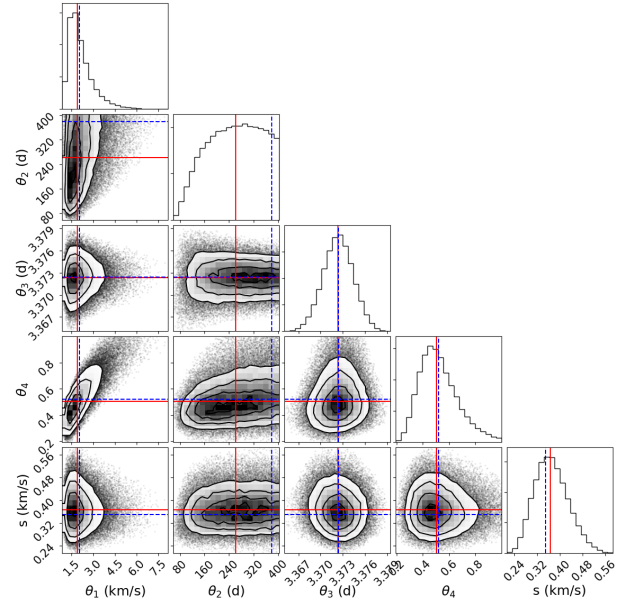


Figure 10. Corner plot of the posterior distribution of the parameters of the GPR given by the MCMC sampling. The median values of the posterior distributions are shown as red solid lines and correspond to the best estimates listed in Table 3. The blue dashed lines depict the values that maximize the log likelihood. This plot was generated with the `CORNER PYTHON` module (Foreman-Mackey 2016).

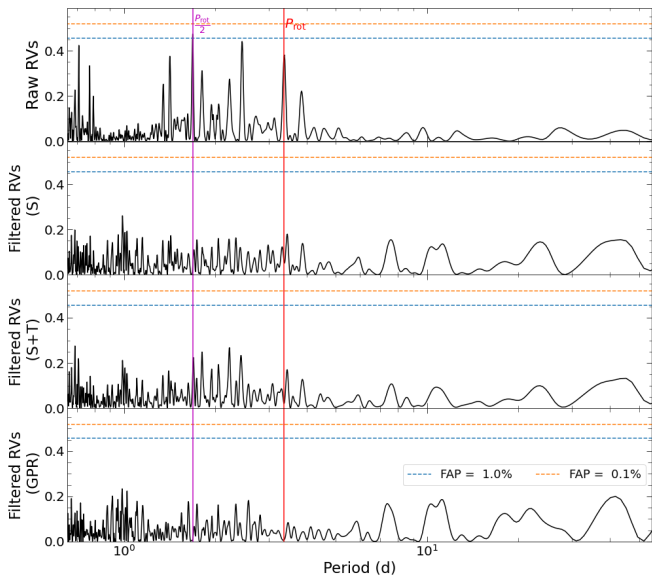


Figure 11. Periodograms of raw radial velocities (1st panel) and filtered radial velocities computed from ZDI brightness reconstructions when using SPIRou (S) data only (2nd panel) or SPIRou and TESS (S+T) data simultaneously (3rd panel) or GPR (4 panel). The red and magenta vertical lines depict P_{rot} and $P_{\text{rot}}/2$. The horizontal dashed lines indicate the FAP levels at 1% and 0.1%. These periodograms were generated using the PYASTRONOMY PYTHON module (Czesla et al. 2019).

5 ACTIVITY INDICATORS

5.1 Equivalent width variations

We focussed on the He I triplet (1083 nm; Fig. B1), the Paschen beta (Pa β ; 1282 nm; Fig. B2) and Brackett gamma (Br γ ; 2165 nm; Fig. B3) lines, known to be proxies of activity in the NIR (e.g. Zirin 1982; Short & Doyle 1998). We see that the Pa β line is blended with a Ca line, which creates a bump in the blue wing of Pa β . However, this feature apparently does not vary more than the continuum and would therefore not impact our analyses.

We computed the equivalent width variations (EWVs) of each line, quantifying the changes in the EW of these lines due to stellar activity, in a way similar to that of Finociety et al. (2021). With this definition, a negative EWV indicates enhanced absorption with respect to the median spectrum. In practice, we first divided each telluric-corrected Stokes I spectrum (top panel of Figs. B1, B2 and B3) by the median one (bottom panel of Figs. B1, B2 and B3) in the stellar rest frame, then computed the EW of the median-divided spectra (middle panel of Figs. B1, B2 and B3), by fitting a Gaussian function of full-width-at-half-maximum set to 55 km s⁻¹ (consistent with the median profile of the lines) centred on the stellar rest frame.

Assuming equal error bars for all spectral points from the dispersion between spectra in the continuum, we found that the average photon-noise uncertainties on the EWVs are equal to 0.7, 0.8 and 2.6 pm for the He I, Pa β and Br γ lines, respectively. As in the case of V410 Tau (Finociety et al. 2021), these error bars are actually underestimated as they do not account for intrinsic variability, e.g., like that induced by activity. We therefore scaled-up all these error bars to ensure a unit χ_r^2 between a periodic fit and the measurements, yielding empirical (and likely pessimist) error bars taking into account photon-noise and intrinsic variability. In practice, the

He I EWVs were fitted with a pure sine wave, while the Pa β EWVs were better modeled with a sine wave including the first harmonic. The Br γ EWVs show no significant variation and are compatible with 0, meaning that no rotationally modulated activity signal is detected in this line. The enhanced uncertainties we obtain are equal to 5.4, 1.9 and 6.6 pm for the He I, Pa β and Br γ EWVs, respectively, i.e., 1.7, 2.4 and 2.5 times larger than the average photon noise ones quoted above.

From the empirical error bars, we can estimate a false alarm probability for the detected modulation. In practice, we fitted a constant instead of a periodic signal to the He I and Pa β EWVs, and we used the empirical error bars to compute the associated χ_r^2 . We find $\chi_r^2 = 1.23$ and 2.80, for the He I and Pa β EWVs, respectively, corresponding to a probability for the detected modulation to be spurious by chance of 0.15 and 10⁻⁸. This indicates that we detected a significant modulation in the Pa β line that shows enhanced absorption around phases 0.3 and 0.7. The He I EWVs show a much less significant modulation, with enhanced absorption around phase 0.4 (see Fig. 12).

5.2 2D Periodograms

We computed 2D periodograms for the He I, Pa β and Br γ lines. We proceeded as in Finociety et al. (2021), i.e. we computed a Generalised Lomb-Scargle Periodogram normalized to 1 following Zechmeister & Kürster (2009), for each velocity bin of the median-divided spectra between -100 and +100 km s⁻¹, thanks to the PYASTRONOMY PYTHON module (Czesla et al. 2019). With this normalization, a value of 1 indicates a perfect sinusoidal fit to the data.

We show the results in Fig. 13, where we see a modulation with a period close to the stellar rotation period for the He I triplet. For the Pa β line, we see a peak in the periodogram at the stellar rotation period but also at half the rotation period (see Fig. 13). The Br γ 2D periodogram does not show any modulation even at half the rotation period. We also see a signal at the stellar rotation period around -85 km s⁻¹ in the He I periodogram, which is most likely related to the modulation of a nearby photospheric Ca line.

These results are consistent with the detected modulation in the EWVs for the He I and Pa β lines. In particular, we see that only one period shows up in the He I periodogram (the associated EWVs being fitted with a pure sine curve) while the Pa β EWVs are fitted with a slightly more complex curve including the fundamental and the first harmonic, with both showing up in the 2D periodogram.

5.3 Autocorrelation matrices

We proceeded as in Finociety et al. (2021) to compute the autocorrelation matrices of the three lines, within an interval of ± 100 km s⁻¹. In particular, using the definition of the unnormalized correlation coefficient given in Finociety et al. (2021) allows one to highlight the relative importance of the correlations. The He I and Pa β matrices are shown in Fig. 14.

We see a clear autocorrelation of the He I triplet and a less obvious one for the Pa β line. The autocorrelation matrix of these two lines shows a slight asymmetry (as the 2D periodograms), the correlation being a bit more pronounced in the blue wing. As for V410 Tau, the Br γ autocorrelation matrices reveals no specific pattern and reflects mainly noise (Finociety et al. 2021).

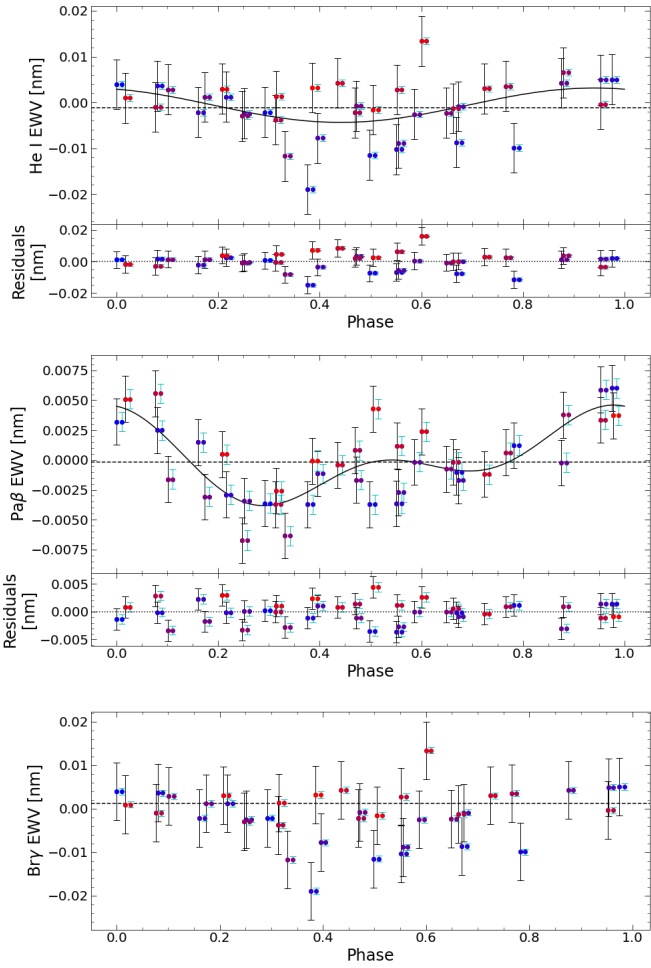


Figure 12. Phase folded activity EWVs derived from the He I triplet at 1083.3 nm (first panel), Pa β (second panel) and Br γ lines (third panel). For the He I and Pa β lines, we show the fit to the data with a periodic function as a solid black line and with a constant as a dotted line in the top plot while the residuals are shown in the bottom plot. For Br γ we only show the fitted constant compatible with 0. In all panels, the cyan error bars are those expected from photon noise (0.7, 0.8 and 2.6 pm) while the black ones are those ensuring a unit χ^2_r fit to the data (5.4, 1.9 and 6.6 pm). The cyan error bars are slightly shifted along the horizontal axis for display purposes. The colour of the dots traces the rotation cycle going from blue (first observation) to red (last observation).

6 SUMMARY AND CONCLUSIONS

Our paper describes results derived from NIR spectropolarimetric data, collected with SPIRou from 2021 Oct 14 to 2022 Jan 30, and photometric observations obtained with TESS between 2021 Sep 16 and Nov 06 and with the ground-based AZT-11 telescope at CrAO between 2021 Oct 10 and 2022 Jan 27, for the wTTS LkCa 4.

6.1 Stellar rotation period and differential rotation

The TESS data show a large amplitude of the light curve in the I_c band (0.3207 ± 0.0006 mag), reflecting the strong activity level of LkCa 4, that remains stable over the 49 d of monitoring. We modeled the very accurate TESS data using a quasi-periodic GP to refine the stellar rotation period, found to be equal to 3.372 ± 0.002 d over our observing window, compatible with a previous estimate (3.374; Grankin et al. 2008). Other indicators derived from SPIRou data,

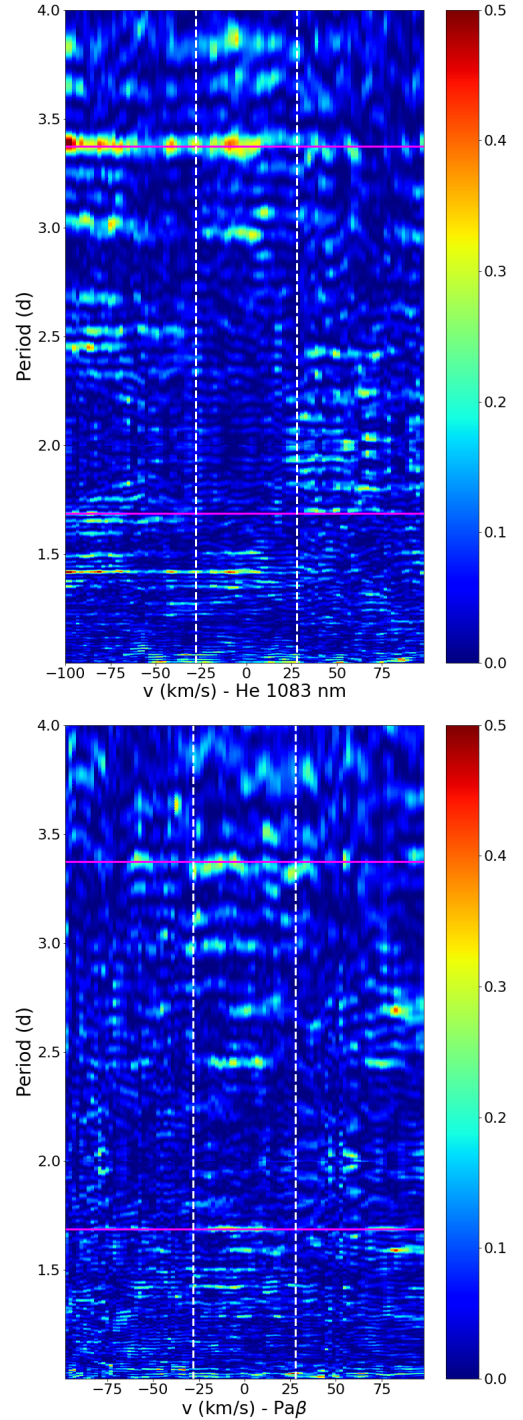


Figure 13. 2D Periododograms of the He I (top) and Pa β (bottom) lines computed with the PYASTRONOMY PYTHON module (Czesla et al. 2019). The magenta line depicts the stellar rotation period and half the rotation period. In both panels, the dashed vertical white lines represents $\pm v \sin i$. The colour bar reflects the power of the Generalized Lomb-Scargle periodogram associated with the period in each velocity bin, being normalized following Zechmeister & Kürster (2009), i.e. with a value of 1 indicating a perfect fit to the data for the corresponding period. The colour bar is limited up to 0.5 for display purposes.

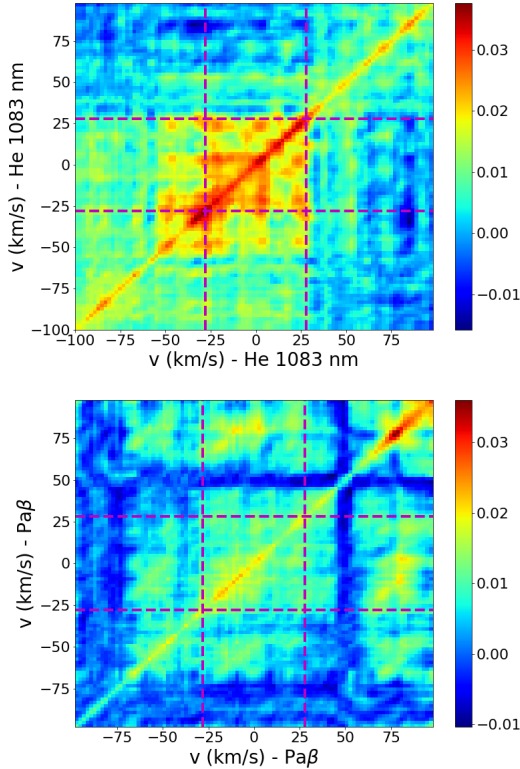


Figure 14. Autocorrelation matrices for He I (top panel) and Pa β (bottom panel). The colorbar refers to the value of the unnormalized coefficients as defined in Finociety et al. (2021) with the scale depending on the level of variability for each of the considered line. Correlations show up in reddish colours while anticorrelation are represented by blueish colours. The dashed magenta lines depicts $\pm v \sin i$.

such as the longitudinal field and the RVs, also yield consistent stellar rotation periods. More specifically, the GPR fit to the RVs provide the same value of 3.372 ± 0.002 d while the longitudinal field measurements suggest a slightly larger value of 3.373 ± 0.002 d, though still compatible.

We also find that the surface of LkCa 4 is sheared by a weak level of DR, 9.5 ± 1.3 times weaker than that of the Sun. In addition, we note that the estimate of the surface DR is much more constrained from our Stokes V LSD profiles, with error bars about 3 times smaller than those derived from Stokes I LSD profiles. Although estimates from optical data are consistent with ours, the error bars derived from SPIRou data (from Stokes I and V) are smaller than those obtained by Donati et al. (2014), up to a factor 30 for Stokes V profiles, which can be largely explained by our larger number of observations (41 with SPIRou vs. 12 with ESPaDOnS) spread over a larger time interval (108 d with SPIRou vs. 13 d with ESPaDOnS) and the benefits of the enhanced Zeeman effect in the NIR (for DR estimates from Stokes V data). We note that our new results indicate that the DR is significantly different from 0 (solid-body rotation) unlike those of Donati et al. (2014).

6.2 Spot coverage

From our brightness reconstructions with ZDI, we found that the stellar surface is covered with spots/plages at a level of about 7% when considering SPIRou data alone, or 9% when including TESS photometry in the fitting process. These values are much lower than

those derived from optical data ($\sim 25\%$; Donati et al. 2014), in agreement with the expected decrease in the brightness contrast of surface features with increasing wavelength. In addition, we do not see a clear polar spot as in ESPaDOnS data, but rather an elongated spot spreading from the pole to the equator around phase 0.1, that could simply result from an evolution of the brightness distribution between 2014 and 2022.

We note that adding TESS photometry in the fitting process increases the spot coverage by $\sim 2\%$, mainly by enhancing the contrasts of brightness features and adding low-latitude structures to ensure that both spectroscopic and photometric data are fitted down to a unit χ_r^2 . This increase is similar to what has been observed for V410 Tau (Finociety et al. 2021) and most likely reflects that spectroscopic and photometric data are not sensitive to the same surface structures.

Our Stokes I LSD profiles show a clear modulation of their EWs with rotation phase (up to 20%), being minimum at phase 0.1 (i.e. when the cool spot is visible) and maximum at phase 0.75 (i.e. when the warm plage is visible). To take into account these variations during the fitting process with ZDI, the depth of the local profiles is allowed to vary as a power δ of the local brightness. Assuming a constant EW (i.e. $\delta = 0$) as in all previous ZDI studies, yields a more contrasted brightness map (spot coverage of $\sim 15\%$) the associated light curve of which in the TESS bandpass has an amplitude twice larger than the observed one. We therefore empirically find that, for this star, $\delta = 1.0 \pm 0.1$ allows us to reproduce the amplitude of the EWs variations as well as the amplitude of the observed light curve. Most of previous ZDI studies dealt with optical data for which variations in EWs are not significant.

ZDI is mostly sensitive to large structures at the surface of the star and misses most of the small features. To estimate the percentage of the visible surface of LkCa 4 covered by dark spots, we used a two-temperature model to fit our $V - I_c$ indexes as a function of the V magnitude, taking into account the visual extinction A_V derived in Donati et al. (2014) and the colour indexes for young stars from Pecaut & Mamajek (2013). We assumed a fixed photospheric temperature of 4140 K and a fixed temperature for the spots, with various filling factors. We found that the $V - I_c$ indexes are consistent with about 70% of the visible surface being covered by spots at 3160 K (Fig. 15) if assuming a unspotted magnitude of 11.97 (as derived from the temperature, distance, radius and visual extinction). The high spot coverage is consistent with the estimate of Gully-Santiago et al. (2017) and similar to what is observed for V410 Tau (Yu et al. 2019; Finociety et al. 2021). However, Gully-Santiago et al. (2017) reported a spot temperature between 2700 and 3000 K, thus lower than our estimate. Our model does not take into account the bright plages which may lead to an overestimate of the temperature of cool spots.

6.3 Magnetic topology

The typical amplitude of our Stokes V LSD profiles (0.5% of the unpolarized continuum) is typically twice smaller than that of optical data collected with ESPaDOnS (1% of the unpolarized continuum, Donati et al. 2014). However, NIR observations, being more sensitive to the magnetic field, provide more accurate measurements than optical data in about half the exposure time. In particular, the larger noise level in our Stokes V LSD profiles (3.4×10^{-4}) corresponds to the typical noise level in the previous optical study (3.5×10^{-4} ; Donati et al. 2014).

We were therefore able to reliably reconstruct the magnetic topology from our set of Stokes I and V LSD profiles. We find that the magnetic topology of LkCa 4 is rather simple and very similar to the one derived from optical data (Donati et al. 2014). The poloidal field

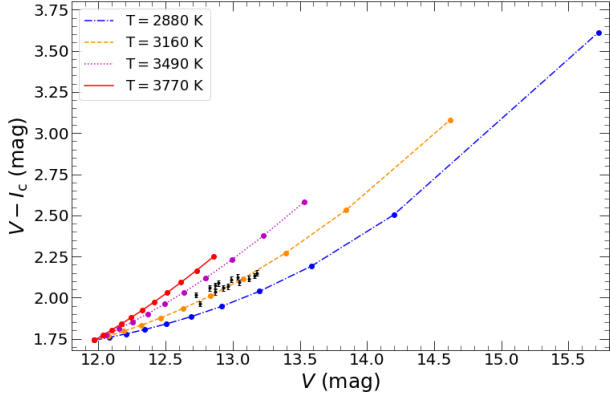


Figure 15. $V - I_c$ colour indexes as a function of the magnitude in the V band, collected from the ground-based AZT-11 telescope at CrAO between 2021 Oct and 2022 Jan. The black dots represent the measurements with the empirical error bars as derived in Sec. 2.2.2. Each colour line represent a two-temperature model with a fixed photospheric temperature of 4140 K and a fixed spot temperature of 2880 (blue dash-dotted line), 3160 (orange dashed line), 3490 (magenta dotted line) and 3770 K (red solid line). Each filled circle corresponds to a different filling factor for the spot with steps of 10%. The unspotted magnitude therefore corresponds to $V = 11.97$. Our data are consistent with spots at 3160 K covering about 70% of the stellar surface.

encloses about 65% of the magnetic energy, consistent with previous estimates. From our data, we estimate that the poloidal field mainly consists of a dipole (of polar strength ~ 2.2 kG, with an axis tilted by $\sim 3^\circ$ with respect to the rotation axis, towards phase 0.31) that concentrates nearly 85% of the poloidal field energy. This dipole is about 35% stronger than the one reconstructed in Donati et al. (2014) and is better aligned with respect to the rotation axis of the star (from 10° in 2014 to 3° in 2021–2022). The toroidal component consists of an equatorial ring of intense azimuthal field, reaching strengths of ~ 1.4 kG. These results suggest that the magnetic topology remained more or less stable over several years with a slight increase in strength. Future observations of LkCa 4 would help to clarify whether the magnetic field of LkCa 4 does significantly evolve with time, e.g., switching overall polarity at times, or is rather in a more or less steady-state dynamo regime.

6.4 Radial velocities

From our Stokes I LSD profiles, we derived RVs of LkCa 4 that show a full amplitude of 6.10 km s^{-1} with a dispersion of 1.45 km s^{-1} . The observed full amplitude is $1.4\times$ larger than the one derived from ESPaDOnS data (Donati et al. 2014). This most likely reflects that the brightness distribution at the surface of LkCa 4 has significantly evolved between 2014 and 2022, generating now a stronger RV activity jitter.

In addition, our typical error bars derived from photon-noise (0.15 km s^{-1}) are $2.5\times$ larger than those derived from ESPaDOnS data (0.06 km s^{-1} ; Donati et al. 2014).

Fitting our RV measurements with a quasi-periodic GP yields an excess of uncorrelated noise of $s = 0.37 \text{ km s}^{-1}$, indicating that the measurements are also affected by stochastic noise (most likely due to stellar activity) that is not taken into account when estimating the error bars from photon noise only.

We first modeled the measured RVs from the ZDI brightness reconstructions. Accounting for TESS photometry in ZDI slightly de-

grades the filtering of the activity jitter as the RMS dispersion of the filtered RVs increases by a factor ~ 1.07 with respect to the model including spectroscopic data only (from 0.45 km s^{-1} to 0.48 km s^{-1}). This effect is not as strong as in the case of V410 Tau for which the RMS dispersion of the filtered RVs varies by a factor ~ 1.8 between both ZDI models (Finocietty et al. 2021). The model associated with the quasi-periodic GP yields a slightly lower RMS dispersion of the filtered RVs of 0.38 km s^{-1} . The RMS dispersions of the filtered RVs obtained from our ZDI models and GPR are about 12 to 16 times smaller than the full amplitude of the measured RVs. The filtering achieved by Donati et al. (2014) using the same method on optical data was better, as the ratio between the full amplitude and the dispersion of their filtered RVs reached a value of 78. The difference most likely reflects the changes in brightness distribution between both epochs, and presumably an increase in the amount of intrinsic variability as well.

We see no significant modulation of all our filtered RVs that would indicate the presence of a close-in massive planet, in agreement with Donati et al. (2014). From simulated data, we estimate that our observations would allow one to detect a planet if the semi-amplitude of its RV signature is larger than 0.44 km s^{-1} and its period is shorter than 50 d. This value is larger than the first estimate by Donati et al. (2014) as the noise level in our data (due to both photon-noise and intrinsic variability) is almost $7\times$ larger. Our threshold typically corresponds to a $4.3 M_{\text{jup}}$ planet at a distance of 0.1 au ($P = 13$ d) or a $6.3 M_{\text{jup}}$ planet at a distance of 0.2 au ($P = 36.8$ d). These upper limits are mainly limited by the high level of intrinsic variability due to stellar activity during the time-span of our data set. More observations would be needed to further assess the potential presence of a close-in massive planet.

6.5 Chromospheric activity

The He I triplet at 1083 nm, the $\text{Pa}\beta$ and $\text{Br}\gamma$ lines were used as proxies of the chromospheric activity of LkCa 4. We first computed the EWVs of the three lines. The He I triplet shows a modulation of its EWVs with rotational cycle (with a probability that this modulation is spurious by chance of 0.15) for which enhanced absorption takes place slightly before the visible pole of the dipole crosses the line-of-sight (phase 0.4) and cannot be related to any magnetic feature. The $\text{Pa}\beta$ EWVs exhibit a more significant modulation for which enhanced absorption (at phase 0.3) may relate to the absorption by wind material escaping the star along open field lines when the pole of the dipole faces the observer. The 2D periodograms further confirms the modulation of the He I and $\text{Pa}\beta$ lines, with in particular half the rotation period showing up in the $\text{Pa}\beta$ 2D periodogram. The He I and $\text{Pa}\beta$ autocorrelation matrices also indicate that an activity signal is detected across the line width.

These results suggest that these two lines react differently to the magnetic field and stellar activity since the modulation of the $\text{Pa}\beta$ line is more significant than that of the He I triplet in contrast to what has been observed for the similar wTTS V410 Tau (Finocietty et al. 2021) and the phased EWV curves of both lines do not match well. However, we find no evidence of a rotationally modulated activity signal in the Br γ line as for V410 Tau (Finocietty et al. 2021). More observations with NIR instruments are needed to investigate whether some trends can be highlighted in the behavior of these three lines in active wTTSs.

6.6 Conclusion

As a follow-up analysis to that of Donati et al. (2014), our study confirms most of the previous results from a completely new data set and wavelength domain. New observations of LkCa 4 are needed to further constrain the evolution of the large-scale magnetic field of this star (e.g. magnetic cycle or steady-state dynamo regime). Observations of other wTTSs with SPIRou, including those targeted within the SLS, will allow one to investigate in details the role that magnetic field plays in the stellar and planetary formation during the transition phase between cTTSs and MS stars. Contemporaneous optical and NIR spectropolarimetric observations of PMS stars would be extremely useful to improve the activity-modelling and jitter-filtering methods, as both domains provide complementary information on stellar activity. Such capabilities would be a key asset for the study of the stellar activity and its impact on the RV data to better characterize planetary systems around active PMS stars like AU Mic (Plavchan et al. 2020; Klein et al. 2021, 2022) and V1298 Tau (David et al. 2019a,b; Suárez Mascareño et al. 2021).

ACKNOWLEDGEMENTS

This work includes data collected in the framework of the SPIRou Legacy Survey (SLS), an international large programme that was allocated on the Canada-France-Hawaii Telescope (CFHT) at the summit of Maunakea by the Institut National des Sciences de l'Univers of the Centre National de la Recherche Scientifique of France, the National Research Council of Canada, and the University of Hawaii. We acknowledge funding by the European Research Council (ERC) under the H2020 research & innovation programme (grant agreements #740651 NewWorlds, #716155 SACCRED, #743029 EASY).

DATA AVAILABILITY

The data collected with TESS are publicly available from the Mikulski Archive for Space Telescopes (MAST) website. The SPIRou data collected as part of the SLS will be publicly available from the CADZ website one year after the completion of the SLS programme, i.e. by mid-2023.

REFERENCES

Alencar S. H. P., et al., 2012, *A&A*, **541**, A116
 Artigau É., et al., 2014, in Peck A. B., Benn C. R., Seaman R. L., eds, Society of Photo-Optical Instrumentation Engineers (SPIE) Conference Series Vol. 9149, Observatory Operations: Strategies, Processes, and Systems V. p. 914905 ([arXiv:1406.6927](https://arxiv.org/abs/1406.6927)), doi:10.1117/12.2056385
 Baraffe I., Homeier D., Allard F., Chabrier G., 2015, *A&A*, **577**, A42
 Bouvier J., Alencar S. H. P., Harries T. J., Johns-Krull C. M., Romanova M. M., 2007, in Reipurth B., Jewitt D., Keil K., eds, Protostars and Planets V. p. 479 ([arXiv:astro-ph/0603498](https://arxiv.org/abs/astro-ph/0603498))
 Bouvier J., et al., 2020, *A&A*, **643**, A99
 Brown S. F., Donati J. F., Rees D. E., Semel M., 1991, *A&A*, **250**, 463
 Claret A., Bloemen S., 2011, *A&A*, **529**, A75
 Crockett C. J., Mahmud N. I., Prato L., Johns-Krull C. M., Jaffe D. T., Hartigan P. M., Beichman C. A., 2012, *ApJ*, **761**, 164
 Czesla S., Schröter S., Schneider C. P., Huber K. F., Pfeifer F., Andreasen D. T., Zechmeister M., 2019, PyA: Python astronomy-related packages (ascl:1906.010)
 David T. J., et al., 2019a, *ApJ*, **158**, 79
 David T. J., Petigura E. A., Luger R., Foreman-Mackey D., Livingston J. H., Mamajek E. E., Hillenbrand L. A., 2019b, *ApJ*, **885**, L12

Donati J. F., 2003, in Trujillo-Bueno J., Sanchez Almeida J., eds, Astronomical Society of the Pacific Conference Series Vol. 307, Solar Polarization. p. 41
 Donati J. F., Brown S. F., 1997, *A&A*, **326**, 1135
 Donati J.-F., Landstreet J. D., 2009, *ARAA*, **47**, 333
 Donati J.-F., Semel M., Carter B. D., Rees D. E., Collier Cameron A., 1997, *MNRAS*, **291**, 658
 Donati J. F., Collier Cameron A., Petit P., 2003, *MNRAS*, **345**, 1187
 Donati J. F., et al., 2006, *MNRAS*, **370**, 629
 Donati J. F., et al., 2007, *MNRAS*, **380**, 1297
 Donati J. F., et al., 2011, *MNRAS*, **412**, 2454
 Donati J. F., et al., 2013, *MNRAS*, **436**, 881
 Donati J. F., et al., 2014, *MNRAS*, **444**, 3220
 Donati J. F., et al., 2017, *MNRAS*, **465**, 3343
 Donati J. F., et al., 2020, *MNRAS*, **491**, 5660
 Finociety B., Donati J.-F., 2022, *Monthly Notices of the Royal Astronomical Society*, **516**, 5887
 Finociety B., et al., 2021, *MNRAS*, **508**, 3427
 Foreman-Mackey D., 2016, *The Journal of Open Source Software*, **1**, 24
 Foreman-Mackey D., Hogg D. W., Lang D., Goodman J., 2013, *PASP*, **125**, 306
 Frank A., et al., 2014, in Beuther H., Klessen R. S., Dullemond C. P., Henning T., eds, Protostars and Planets VI. p. 451 ([arXiv:1402.3553](https://arxiv.org/abs/1402.3553)), doi:10.2458/azu_uapress_9780816531240-ch020
 Gaia Collaboration et al., 2021, *A&A*, **649**, A1
 Grankin K. N., 2013, *Astronomy Letters*, **39**, 251
 Grankin K. N., Bouvier J., Herbst W., Melnikov S. Y., 2008, *A&A*, **479**, 827
 Gregory S. G., Donati J. F., Morin J., Hussain G. A. J., Mayne N. J., Hillenbrand L. A., Jardine M., 2012, *ApJ*, **755**, 97
 Gully-Santiago M. A., et al., 2017, *ApJ*, **836**, 200
 Herbig G. H., Vrba F. J., Rydgren A. E., 1986, *AJ*, **91**, 575
 Jenkins J. M., et al., 2016, in Software and Cyberinfrastructure for Astronomy IV. p. 99133E, doi:10.1117/12.2233418
 Klein B., et al., 2021, *MNRAS*, **502**, 188
 Klein B., et al., 2022, *MNRAS*, **512**, 5067
 Kraus A. L., Ireland M. J., Martinache F., Hillenbrand L. A., 2011, *ApJ*, **731**, 8
 Krolikowski D. M., Kraus A. L., Rizzuto A. C., 2021, *AJ*, **162**, 110
 Landi Degl'Innocenti E., Landolfi M., 2004, *Polarisation in Spectral Lines*. Kluwer Academic Publishers, Dordrecht
 Mahmud N. I., Crockett C. J., Johns-Krull C. M., Prato L., Hartigan P. M., Jaffe D. T., Beichman C. A., 2011, *ApJ*, **736**, 123
 Morin J., et al., 2008, *MNRAS*, **390**, 567
 Morin J., Donati J.-F., Petit P., Delfosse X., Forveille T., Jardine M. M., 2010, *MNRAS*, **407**, 2269
 Pecaat M. J., Mamajek E. E., 2013, *ApJS*, **208**, 9
 Plavchan P., et al., 2020, *Nature*, **582**, 497
 Rajpaul V., Aigrain S., Osborne M. A., Reece S., Roberts S., 2015, *MNRAS*, **452**, 2269
 Rasmussen C., Williams C., 2006, *Gaussian Processes for Machine Learning. Adaptive Computation and Machine Learning*, MIT Press, Cambridge, MA, USA
 Ricker G. R., et al., 2014, in Space Telescopes and Instrumentation 2014: Optical, Infrared, and Millimeter Wave. p. 914320 ([arXiv:1406.0151](https://arxiv.org/abs/1406.0151)), doi:10.1117/12.2063489
 Ryabchikova T., Piskunov N., Kurucz R. L., Stempels H. C., Heiter U., Pakhomov Y., Barklem P. S., 2015, *Phys. Scr.*, **90**, 054005
 Semel M., 1989, *A&A*, **225**, 456
 Short C. I., Doyle J. G., 1998, *A&A*, **331**, L5
 Siess L., Dufour E., Forestini M., 2000, *A&A*, **358**, 593
 Smith J. C., et al., 2012, *PASP*, **124**, 1000
 Stumpe M. C., et al., 2012, *PASP*, **124**, 985
 Stumpe M. C., Smith J. C., Catanzarite J. H., Van Cleve J. E., Jenkins J. M., Twicken J. D., Girouard F. R., 2014, *PASP*, **126**, 100
 Suárez Mascareño A., et al., 2021, *Nature Astronomy*, **6**, 232
 White R. J., Ghez A. M., 2001, *ApJ*, **556**, 265
 Yu L., et al., 2017, *MNRAS*, **467**, 1342
 Yu L., et al., 2019, *MNRAS*, **489**, 5556

Table A1. Ground-based photometric observations of LkCa 4 collected with the AZT-11 telescope at CrAO between 2021 October and 2022 January. The 1st and 2nd columns list the date and the Heliocentric Julian Date. In column 3, we give the measured magnitude in the *V* band. Columns 4 and 5 report the colour indexes $V - R_J$, $V - I_J$ in the Johnson system while columns 6 and 7 detail the colour indexes $V - R_c$ and $V - I_c$ in the Cousins system.

Date	HJD 2459000+	<i>V</i> (mag)	$V - R_J$ (mag)	$V - I_J$ (mag)	$V - R_c$ (mag)	$V - I_c$ (mag)
2021 October 10	498.417	12.932	1.515	2.624	1.053	2.059
2021 October 17	505.509	13.121	1.498	2.696	1.041	2.115
2021 October 30	518.519	12.868	1.556	2.594	1.083	2.035
2021 November 03	522.524	13.181	1.575	2.740	1.096	2.150
2021 November 10	529.514	13.160	1.560	2.718	1.086	2.133
2021 November 11	530.521	12.987	1.559	2.689	1.085	2.110
2021 November 12	531.535	12.728	1.539	2.569	1.071	2.016
2021 November 15	534.519	12.830	1.578	2.622	1.099	2.058
2021 November 16	535.535	12.963	1.520	2.637	1.057	2.069
2021 December 02	551.219	12.891	1.570	2.662	1.093	2.088
2021 December 10	559.187	13.037	1.580	2.708	1.100	2.125
2021 December 23	572.321	12.758	1.475	2.501	1.025	1.963
2022 January 25	605.247	12.871	1.568	2.641	1.091	2.073
2022 January 27	607.306	13.050	1.543	2.667	1.074	2.093

Zechmeister M., Kürster M., 2009, *A&A*, 496, 577

Zirin H., 1982, *ApJ*, 260, 655

APPENDIX A: JOURNAL OF OBSERVATIONS FOR GROUND-BASED PHOTOMETRY

We provide a full journal for the observations collected with the ground-based AZT-11 telescope at CrAO in Table A1.

APPENDIX B: HE I, PA β AND BR γ SPECTRA

We show the telluric-corrected spectra, median spectrum and median-divided spectra for the He I (Fig. B1), Pa β (Fig. B2) and Br γ (Fig. B3) lines, used as proxies to investigate the chromospheric activity of LkCa 4.

This paper has been typeset from a \LaTeX file prepared by the author.

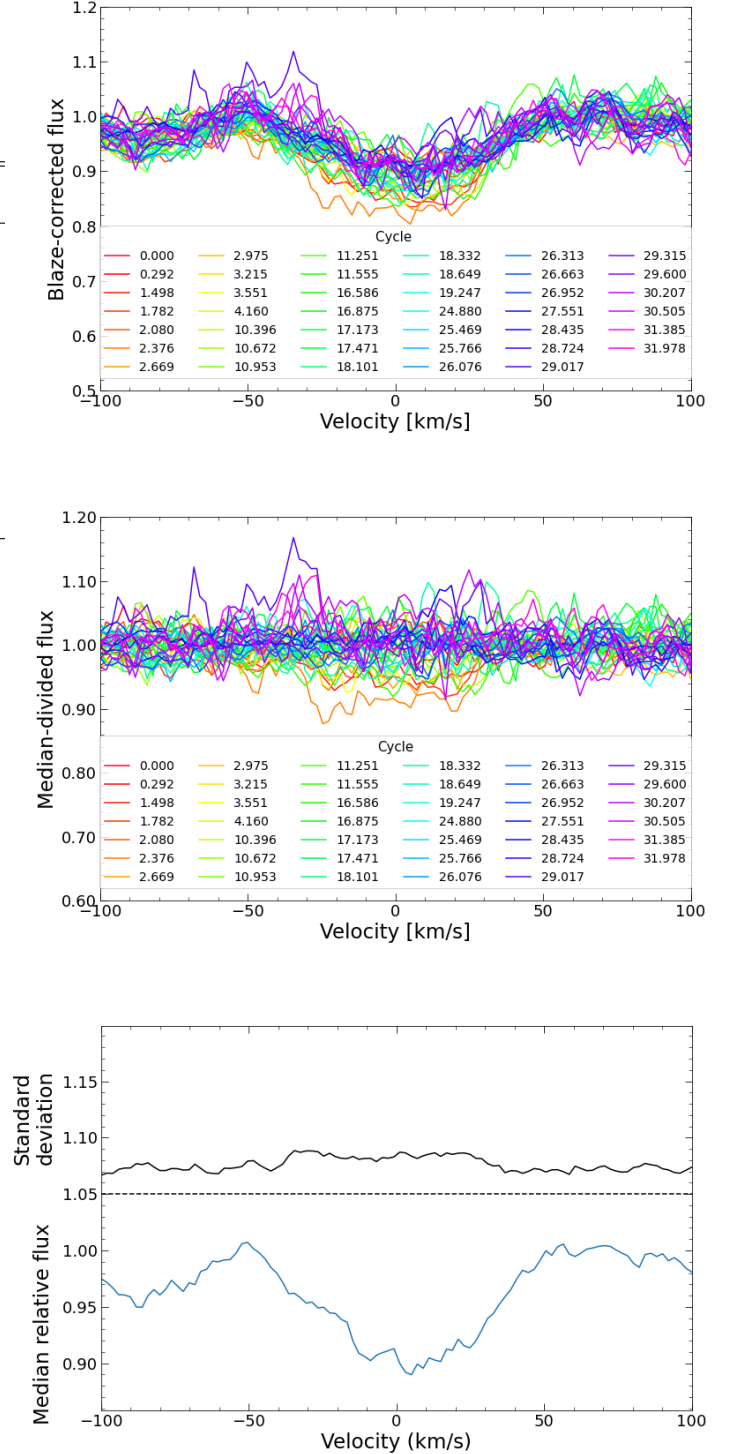


Figure B1. Telluric corrected profiles (top), median-divided profiles (middle) and median profile (bottom) for the He I triplet. In the bottom panel, the dispersion in the velocity bins of the median-divided spectra is shown in solid black line, shifted upwards by 1.05 for display purposes while the dashed line depicts the zero variability level.

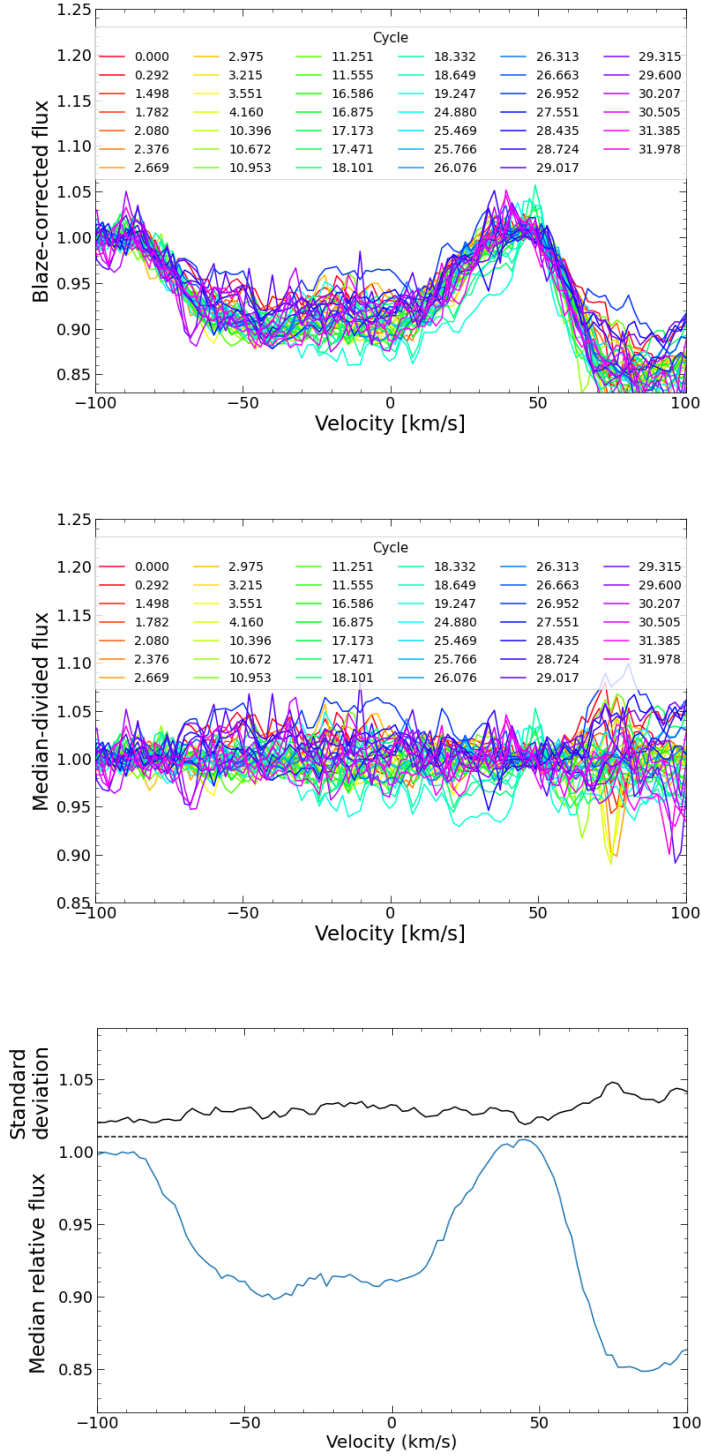


Figure B2. Same as Fig. B1 for the Pa β line. In the bottom panel, the zero variability level is shifted upwards by 1.01 for clarity purposes. In addition, we see that the blue wing of the line is blended, likely with a Ca line, causing the depression around -50 km s^{-1} .

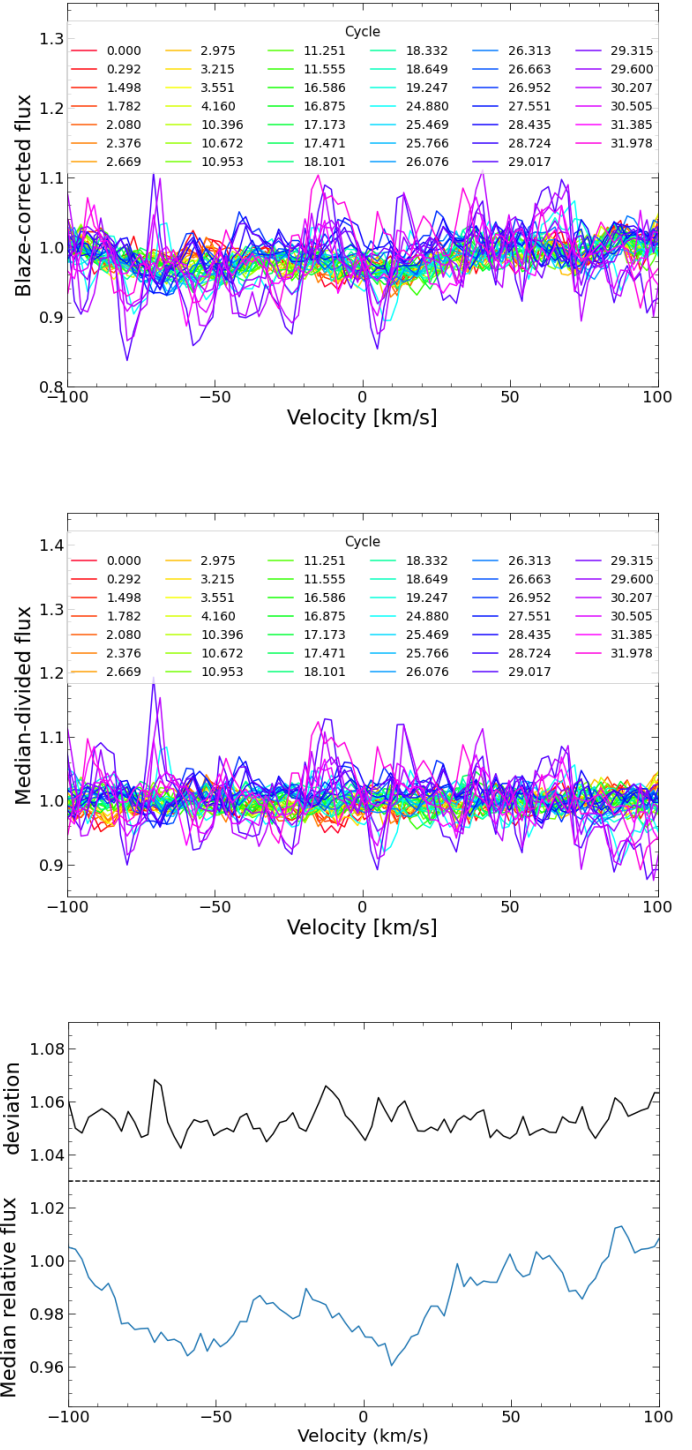


Figure B3. Same as Fig. B1 for the Br β line. In the bottom panel, the zero variability level is shifted upwards by 1.03 for clarity purposes. We see essentially noise in this line.